

# Trapped acoustic waves and raindrops: high-order accurate integral equation method for localized excitation of a periodic staircase

Fruzsina J. Agocs<sup>a,\*</sup>, Alex H. Barnett<sup>a</sup>

<sup>a</sup>*Center for Computational Mathematics, Flatiron Institute, 162 Fifth Avenue, New York, NY, USA*

---

## Abstract

We present a high-order boundary integral equation (BIE) method for the frequency-domain acoustic scattering of a point source by a singly-periodic, infinite, corrugated boundary. We apply it to the accurate numerical study of acoustic radiation in the neighborhood of a sound-hard two-dimensional staircase modeled after the *El Castillo* pyramid. Such staircases support trapped waves which travel along the surface and decay exponentially away from it. We use the array scanning method (Floquet–Bloch transform) to recover the scattered field as an integral over the family of quasiperiodic solutions parameterized by on-surface wavenumber. Each such BIE solution requires the quasiperiodic Green’s function, which we evaluate using an efficient integral representation of lattice sum coefficients. We avoid the singularities and branch cuts present in the array scanning integral by complex contour deformation. For each frequency, this enables a solution accurate to around 10 digits in a couple of seconds. We propose a residue method to extract the limiting powers carried by trapped modes far from the source. Finally, by computing the trapped mode dispersion relation, we use a simple ray model to explain an observed acoustic “raindrop” effect (chirp-like time-domain response).

---

## 1. Introduction

Periodic surface geometries have long been exploited to manipulate electromagnetic and acoustic waves. Examples on small and large length-scales include photonic crystals [1, 2], acoustic metamaterials [3, 4], diffraction gratings [5], antennae [6, 7], anechoic chambers and materials [8], and amphitheatres [9]. However, the accurate numerical solution of radiation near such geometries faces several challenges. The domain—a perturbation of the upper half-space—is unbounded vertically, thus its truncation must incorporate the correct upward-going radiation conditions. The possibility of coupling to waves trapped *along* the surface, which in two dimensions (2D) do not decay at all, means that  $\mathcal{O}(1)$  reflection errors would result by naive truncation to any finite number of unit cell periods. These trapped waves may also cause resonances with high parameter sensitivity [10]. Having non-periodic excitation breaks the periodicity of the

---

\*corresponding author.

*Email addresses:* fagocs@flatironinstitute.org (Fruzsina J. Agocs),  
 abarnett@flatironinstitute.org (Alex H. Barnett)

problem, which makes periodization impossible at first glance. However, it is possible to deconstruct the single point-source solution into sets of quasiperiodic solutions (the array scanning or Floquet–Bloch method). As in any wave problem, high frequencies may demand a large discretization density [11]. Finally, the staircase model that we focus on here introduces corner singularities that must be addressed in any high-order solver. Since solvers are often part of a design optimization loop to tune material or shape parameters, they must be robust and efficient. However, the above difficulties mean that nonconvergent Rayleigh expansions [12], or ray asymptotic methods [13] are often used in acoustic settings.

The purpose of this paper is twofold: 1) We present a high-order numerical boundary integral (BIE) method for 2D acoustic scattering of a point source from a singly-periodic geometry, in particular combining it with a high-order accurate array scanning method via contour deformation. 2) We apply this to the accurate numerical study of acoustic radiation in the neighborhood of a sound-hard 2D staircase model, in order to understand time- and frequency-domain phenomena due to nearby point-source excitation. For the time-domain we compute the dispersion relation of trapped modes and use it to explain an observed chirp effect [14, 15]; for the frequency domain we propose a method to extract the amplitudes of the left- and right-going trapped modes, using residues in the complexified on-surface wavenumber. Architecturally, solid staircases with sound-hard surfaces are clearly very common; yet, we have not found an accurate numerical study of acoustic trapping and guiding in their vicinity. By combining high-order corner quadratures and lattice sums, we show that a BIE can achieve around 10 digits of accuracy with solution times of a couple of seconds per excitation frequency.

We consider a 2D model for linearized acoustics in a simply-connected region  $\Omega \subset \mathbb{R}^2$  containing a constant-density gas with constant sound speed  $c > 0$  [16, 17], [18, Sec. 3.1]. This region lies above a connected corrugated boundary  $\partial\Omega$  extending with spatial period  $d$  in the  $x_1$  direction, and is unbounded in the positive  $x_2$  direction; see fig. 1. The boundary has a maximum and minimum  $x_2$  coordinate. Our paradigm example will be the slope- $\pi/4$  right-angle staircase shown in the figure, whose repeating element (unit cell) comprises two equal-length line segments at an angle  $\pi/2$  to each other. We write  $\mathbf{x} = (x_1, x_2)$ . This models a 3D situation in which both geometry and source are invariant in the 3rd (out of plane) direction.

The tools we present mostly concern frequency domain solutions, but we will also use them to understand a chirp phenomenon for the following time domain problem. Consider an impulse excitation by a point source at time  $t = 0$  and location  $\mathbf{x}_0 \in \Omega$ ; this is a good model for a clap or footstep in the acoustic application. The acoustic pressure  $U(t, \mathbf{x})$  then obeys the wave equation with a source,

$$\frac{\partial^2 U(t, \mathbf{x})}{\partial t^2} - \Delta U(t, \mathbf{x}) = \delta(t)\delta(\mathbf{x} - \mathbf{x}_0), \quad t \in \mathbb{R}, \quad \mathbf{x} \in \Omega, \quad (1)$$

where  $\Delta = \nabla \cdot \nabla$  is the spatial Laplacian, and by a rescaling of time  $t$  we set the sound speed to  $c = 1$ . We assume quiescence before the excitation:  $U \equiv 0$  for  $t < 0$ .<sup>1</sup> The sound-hard (Neumann) boundary condition is

$$U_n(t, \mathbf{x}) = 0, \quad t \in \mathbb{R}, \quad \mathbf{x} \in \partial\Omega, \quad (2)$$

where  $U_n := \mathbf{n} \cdot \nabla U$  is the normal derivative,  $\mathbf{n}$  being the unit boundary normal vector pointing into  $\Omega$ . This arises physically since the normal component of the fluid velocity vanishes; it is a good approximation to an air-solid interface [19, Ch. 1].

---

<sup>1</sup>Note that (1) could thus be rephrased as the homogeneous wave equation in  $t > 0$  with initial conditions  $U(0, \cdot) \equiv 0$ ,  $U_t(0, \cdot) = \delta_{\mathbf{x}_0}$ .

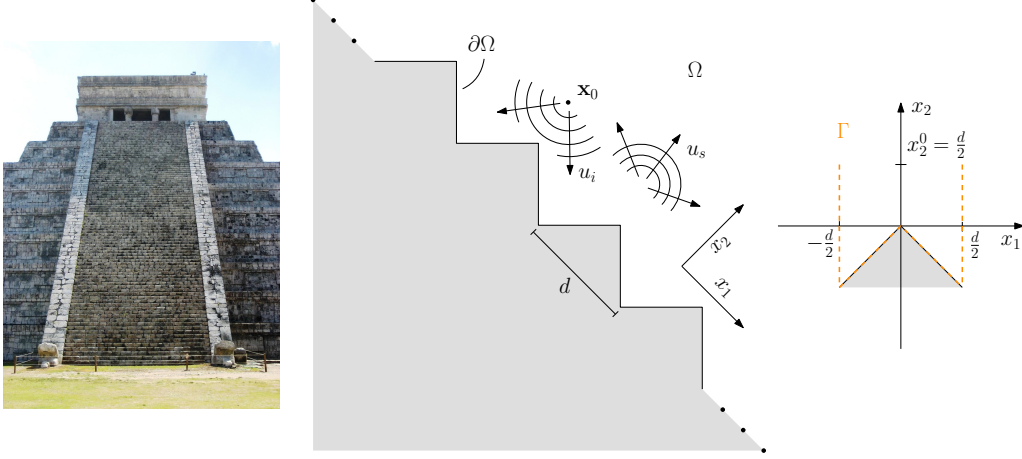


Figure 1: Left: Photograph of *El Castillo* at Chichen Itza, Mexico. Center: 2D infinite staircase geometry with coordinates used. Right: a single period  $\Gamma$  of the boundary, now shown with  $x_1$  horizontal (the orientation used throughout).

Taking the Fourier transform of (1) and (2) with respect to  $t$  gives the main focus of this paper, the inhomogeneous Helmholtz Neumann boundary value problem (BVP),

$$-(\Delta + \omega^2)u = \delta_{\mathbf{x}_0} \quad \text{in } \Omega, \quad (3)$$

$$u_n = 0 \quad \text{on } \partial\Omega, \quad (4)$$

and radiation conditions explained below. Here  $\omega \in \mathbb{R}$  is the frequency, and the wavelength is  $2\pi/\omega$ . From the  $\omega$ -dependence of its solution  $u$  one may understand features of the above time-domain solution  $U$ .

The remainder of this extended Introduction sets up definitions needed to convert section 1 into BVPs posed on a bounded unit cell, and overviews the rest of the paper. The solution to section 1 may be decomposed into a linear combination of *quasiperiodic* solutions, via what is known as the array scanning method in the engineering literature [6, 20, 21], or inverse Floquet–Bloch transform in mathematics [22, 23]. This family of quasiperiodic solution is parameterized by  $\kappa \in \mathbb{R}$ , the horizontal (along-surface) wavenumber, and each member of the family has the phased translational symmetry  $u_\kappa(x_1 + nd, x_2) = \alpha^n u_\kappa(x_1, x_2)$ , for all  $n \in \mathbb{Z}$  and  $\mathbf{x} \in \Omega$ , where the *Bloch phase* is  $\alpha = e^{i\kappa d}$ . The set of *plane waves* of the form  $e^{i\mathbf{k}\cdot\mathbf{x}}$  obeying the homogeneous Helmholtz equation and quasiperiodic symmetry is discrete, namely  $\mathbf{k}_n = (\kappa_n, k_n)$ , where

$$\kappa_n := \kappa + 2\pi n/d, \quad n \in \mathbb{Z} \quad (5)$$

is the shifted lattice of horizontal wavenumbers with the same  $\alpha$ , and

$$k_n := +\sqrt{\omega^2 - \kappa_n^2} \quad (6)$$

is the vertical wavenumber.  $k_n$  is either positive real (upwards-propagating), zero (horizontally propagating), or positive imaginary (upwards-decaying).

Then, for a given  $\kappa$ , the quasiperiodic solution  $u = u_\kappa$  solves the BVP

$$-(\Delta + \omega^2)u = f_\kappa \quad \text{in } \Omega, \quad (PDE) \quad (7)$$

$$u_n = 0 \quad \text{on } \partial\Omega, \quad (\text{boundary condition}) \quad (8)$$

$$u(x_1 + d, x_2) = \alpha u(x_1, x_2) \quad (x_1, x_2) \in \Omega, \quad (\text{quasiperiodicity}) \quad (9)$$

$$u(x_1, x_2) = \sum_{n \in \mathbb{Z}} c_n e^{i(\kappa_n x_1 + k_n x_2)}, \quad x_2 > x_2^0, \quad (\text{radiation condition}) \quad (10)$$

where  $x_2^{(0)}$  is any height lying above the support of the source and above  $\partial\Omega$ , and  $c_n$  are amplitudes of the outgoing plane waves. The source  $f_\kappa$  must naturally also be quasiperiodic: it is a quasiperiodized version of the desired right-hand side  $\delta(\mathbf{x} - \mathbf{x}_0)$ , namely

$$f_\kappa(\mathbf{x}) := \sum_{n=-\infty}^{\infty} e^{i\kappa n d} \delta(\mathbf{x} - \mathbf{x}_0 - n\mathbf{d}), \quad (11)$$

where  $\mathbf{d} := (d, 0)$  is the lattice vector. Fixing  $\omega > 0$ , the above BVP has a unique solution for all  $\kappa \in \mathbb{R}$  apart from possibly a discrete set (which will correspond to trapped modes, and discussed in detail in section 3) [24]. The above also extends to  $\kappa \in \mathbb{C}$ ; see [10, Sec. 4.1].

Each member  $u_\kappa$  of the above quasiperiodic solution family is the acoustic response of the periodic geometry to an infinite array of phased point sources. The key observation (giving ‘‘array scanning’’ its name) is that one may cancel out all but the central source by integration over  $\kappa$  in the first Brillouin zone:

$$\delta(\mathbf{x} - \mathbf{x}_0) = \frac{d}{2\pi} \int_{-\pi/d}^{\pi/d} f_\kappa(\mathbf{x}) d\kappa. \quad (12)$$

This exploits the fact that  $\int_{-\pi/d}^{\pi/d} e^{i\kappa n d} d\kappa = 2\pi/d$  for  $n = 0$ , and zero for  $n \in \mathbb{Z}, n \neq 0$ . Since this is the right-hand side in (7), then, by linearity, performing the same integral over the solution family  $u_\kappa$ ,

$$u(\mathbf{x}) = \frac{d}{2\pi} \int_{-\pi/d}^{\pi/d} u_\kappa(\mathbf{x}) d\kappa \quad (13)$$

recovers  $u$ , the solution to (7) and (18) with upward-propagating radiation conditions.

**Remark 1.** *In the case where  $u_\kappa$  is not unique for some discrete real  $\kappa$  values, the integral (13) has poles on the real axis corresponding to evanescent waves trapped on the corrugated surface. General conditions for existence of such Neumann boundary condition trapped modes are not known [25, p.11–12], although they are well known, and proven to exist for certain geometries [26, 27]. The mathematical formulation of causal outgoing radiation conditions in the presence of trapped modes is subtle, relying on the limiting absorption principle (for dielectric cases see [28, 29]). We did not find the sound-hard case in the literature, but, following Zhang [23], we define this by the topology of the integration contour with respect to the poles. This is presented in section 4.*

The integration interval  $\kappa \in [-\pi/d, \pi/d]$  is known as the *first Brillouin zone*, and covers the family of solutions. This is because  $u_\kappa$  is the same for all  $\kappa$  in the set (5) (since  $\alpha$  is the same, and so is the set of plane waves in the radiation condition, up to relabeling). The integration may also be thought of as over  $\alpha$  on the unit circle [23]. We present a high-order accurate quadrature method for the above integral (13). This is crucial for efficiency, because each such quadrature

node demands a new BVP solution of (7) to (10). Here, care is needed due to the possibility of poles mentioned in the above remark, but also because the integrand contains two square-root singularities (with associated branch cuts) at so-called (*Rayleigh–Wood anomalies* [30, 31, 32]). These anomalies are defined as pairs  $(\omega, \kappa)$  where  $k_n = 0$  for some  $n \in \mathbb{Z}$  in (6) (see fig. 2), resulting in a horizontal plane wave. Although the quasiperiodic BVP remains well-posed, it poses challenges for Green’s function based numerical methods [33, 34, 35, 36, 37]. Following Zhang [23] in the setting of closed waveguides, we propose contour deformation to complex  $\kappa$  to avoid such anomalies and poles. Rather than the piecewise-smooth contours of that work, we use a more efficient analytic contour deformation, and optimize a deformation parameter to minimize the number of nodes needed; see section 4.

Boundary integral equation (BIE) methods [18, 38] are especially suited for the high-order accurate solution of each quasiperiodic BVP. Since they operate by first converting the PDE to a boundary integral, then discretizing it to yield a dense linear system, they only require the evaluation of a 1D integral instead of the discretization of a (truncated) infinite 2D domain. This reduction of dimensionality significantly reduces the number of unknowns, and allows for an easy increase in order of accuracy via high-order quadrature rules. Furthermore, the staircase geometry has two corners per period, one of which induces fractional-power-law singularities in  $u$ ; these are easily handled with BIE. In contrast, a finite differencing (FD) or finite elements (FEM) would require meshing of the domain in a manner respecting the corner singularity, and explicit handling of the radiation condition (10). Both FD [22] and FEM [39] have been combined with array scanning to solve the scattering from periodic surfaces, but using only low-order spatial discretization.

There exist other boundary-based approaches. These include meshfree methods such as the method of fundamental solutions (MFS) [40, 41, 42], and the plane waves method [43]. These share common roots with BIE methods in that the solution is constructed from Helmholtz solutions in the domain, but generally give ill-conditioned systems. For scattering by periodic surfaces, a family of methods exists based on the Rayleigh hypothesis (Rayleigh methods) [44, p. 17], [45]. These assume that an expansion of the scattered field like (10) is valid close to and on the surface, and approximate the solution as a truncation of (10). This assumption, however, does not generally hold. Fast approximate solutions are most commonly derived using the Helmholtz–Kirchhoff approximation [46], which assumes that each point on the boundary scatters as if it was a plane at a slope matching that of the boundary. This represents a short-wavelength limit and is closely related to the geometrical acoustics [47, 48]; its validity has been studied thoroughly [12].

To use boundary integral methods, one splits the physical solution as  $u = u_i + u_s$ , where the *incident wave*  $u_i$  solves (7) with free-space radiation conditions and no boundary conditions, and is thus known analytically, whilst the unknown *scattered wave*  $u_s$  solves the homogeneous version of (7), with inhomogeneous boundary condition  $(u_s)_n = -(u_i)_n$  on  $\partial\Omega$ , and (9) and (10). A BIE is then used to solve this BVP for  $u_s$ , as presented in section 2.

A BIE formulation on the infinite surface  $\partial\Omega$  would not be numerically feasible, and its truncated solution converges very slowly since the contributions of distant sources decay only like  $1/\sqrt{r}$ . However, the computation of the quasiperiodic solution may be reduced to a single unit cell of the boundary. This periodization process involves replacing in the integral kernels the free-space Green’s function  $\Phi(\mathbf{x})$ , defined as the radiative solution to

$$-(\Delta + \omega^2)\Phi(\mathbf{x}) = \delta(\mathbf{x}), \quad (14)$$

with the quasiperiodic Green’s function  $\Phi_p(\mathbf{x})$  defined as the upwards- and downwards-radiating

solution to

$$-(\Delta + \omega^2)\Phi_p(\mathbf{x}) = \sum_{n=-\infty}^{\infty} \alpha^n \delta(x_1 - nd)\delta(x_2). \quad (15)$$

The periodic Green’s function is therefore an infinite phased sum of single point-source Green’s functions. The sum is slowly convergent and cannot be used directly [49]. Yet a wide range of methods exist for the rapidly-convergent approximation of  $\Phi_p$ , including reformulation in terms of quickly convergent lattice sums [50]. In section 2.1, we discuss one such efficient computation of  $\Phi_p$  based on [51]. By the use of contour deformation to complex  $\kappa$ , we will avoid Wood anomalies where (15) does not exist.

With the periodic Green’s function in hand, section 2.2 describes the boundary layer representation of the solution and the discretization of the boundary, including the treatment of the singularities present in the boundary integral at the corners of the boundary. In general, these may be handled analytically, *e.g.* via Gauss–Jacobi quadrature [52], or conformal mapping [53]; or handled to high order by generalized Gauss quadrature [54], recursive compressed inverse preconditioning [55], or rational function approximation [56]. In section 2.3 that follows, we describe how the total field is reconstructed outside the unit cell, and verify the high-order accuracy of the solution with convergence tests which exploit flux conservation.

**Remark 2.** *A distributed spatial source (right-hand side in (7)) may also be handled by a slight generalization of our framework: one numerically computes their incident wave  $u_i$  by convolution of the source function with  $\Phi_p$ . The BIE solutions for  $u_s$  then proceed as before.*

In section 3 we will show how numerically to locate eigenparameters  $(\omega, \kappa)$  for which trapped modes exist. Such modes are eigenfunctions, *i.e.*, nontrivial homogeneous solutions to the BVP (7) to (10). As remark 1 implied, at each  $\omega$ , such  $\kappa$  values are vital to know since they induce poles in the array scanning (inverse Floquet–Bloch) integral. Yet, the mode *dispersion relation*—the dependence of  $\omega$  vs  $\kappa$  for trapped modes—also will provide a model to understand the “raindrop effect” (chirp-like response) for the time-domain problem (1) and (2). For this reason, we present a strategy to solve for the trapped  $\omega$  at a given  $\kappa$ . This involves rootfinding on the Fredholm determinant of the  $\omega$ -dependent integral operator, as done in [57]. A trapped mode may be reconstructed from the eigenfunction of the Fredholm 2nd-kind integral equation. From the dispersion relation, we derive their group velocities; the speed at which a given trapped mode propagates along the surface. We use an approximate ray model (neglecting amplitudes) to predict the arrival times of different frequencies at the bottom of a staircase modeled after the *El Castillo* pyramid, in order to understand the chirp-like sounds observed.

We also pose, and answer in Section 5, the following: how can one efficiently use the array scanning method to report the power carried away by (left- or right-going) trapped modes, as opposed to power radiated upwards away from the surface? Characterizing this division of radiated power as a function of frequency is crucial in related engineering applications such as point-source radiators in nanophotonics and acoustic metamaterials. Finally, we discuss avenues for future work in section 6.

## 2. BIE formulation, periodization, and discretization

Here we present the numerical method for solving the quasiperiodic BVP (7) to (10), at a given  $\omega > 0$  and  $\kappa \in \mathbb{C}$ . The physical wave (potential) is written  $u = u_i + u_s$ . Fixing the source

$\mathbf{x}_0 \in \mathbb{R}^2$ , we take the incident wave to be the quasiperiodic function

$$u_i(\mathbf{x}) = \Phi_p(\mathbf{x}, \mathbf{x}_0), \quad \mathbf{x} \in \mathbb{R}^2, \quad (16)$$

where we use the notation  $\Phi_p(\mathbf{x}, \mathbf{y}) = \Phi_p(\mathbf{x} - \mathbf{y})$ , recalling (15). The PDE and boundary condition for  $u$  (7) and (8) imply that  $u_s$  solves the BVP

$$(\Delta + \omega^2)u_s = 0 \quad \text{in } \Omega, \quad (17)$$

$$(u_s)_n = -(u_i)_n \quad \text{on } \partial\Omega, \quad (18)$$

with  $u_s$  obeying the quasiperiodicity and radiation conditions (9) and (10). Since the PDE is now homogeneous, a BIE solution becomes possible.

The unknown scattered field  $u_s$  is represented by a quasiperiodic single-layer potential

$$u_s(\mathbf{x}) = (\mathcal{S}\sigma)(\mathbf{x}) := \int_{\Gamma} \Phi_p(\mathbf{x}, \mathbf{y})\sigma(\mathbf{y})ds_{\mathbf{y}}, \quad \mathbf{x} \in \mathbb{R}^2, \quad (19)$$

where the usual fundamental solution  $\Phi(\mathbf{x}, \mathbf{y})$  has been replaced with its quasiperiodic counterpart, and  $\Gamma := \partial\Omega \cap \{|x_1| \leq d/2\}$  is a single unit cell (period) of the boundary. As  $\mathbf{x}$  approaches the boundary from either side, let us define

$$u_s^{\pm}(\mathbf{x}) := \lim_{h \rightarrow 0^{\pm}} u_s(\mathbf{x} + h\mathbf{n}_{\mathbf{x}}), \quad \mathbf{x} \in \Gamma, \quad (20)$$

$$(u_s)_n^{\pm}(\mathbf{x}) := \lim_{h \rightarrow 0^{\pm}} \mathbf{n}_{\mathbf{x}} \cdot \nabla u_s(\mathbf{x} + h\mathbf{n}_{\mathbf{x}}), \quad \mathbf{x} \in \Gamma. \quad (21)$$

Here  $\mathbf{n}_{\mathbf{x}}$  is the unit normal to the boundary at the target point  $\mathbf{x}$ . The above representation then satisfies the jump relations (see [38, Ch 6.3])

$$u_s^{\pm} = \mathcal{S}\sigma, \quad \text{on } \Gamma, \quad (22)$$

$$(u_s)_n^{\pm} = \left(D^T \mp \frac{1}{2}I\right)\sigma, \quad \text{on } \Gamma, \quad (23)$$

where  $D^T$  denotes the adjoint double-layer operator on  $\Gamma$ , namely the operator with kernel  $\partial\Phi_p(\mathbf{x}, \mathbf{y})/\partial\mathbf{n}_{\mathbf{x}}$  taken in the principal value sense.

The single-layer representation for  $u_s$  automatically satisfies (17), and the boundary condition can be written in terms of the single-layer jump condition as

$$(I - 2D^T)\sigma = 2(u_i)_n \quad \text{on } \Gamma. \quad (24)$$

This is a Fredholm integral equation of the second kind.

**Remark 3.** *The expert reader may wonder why a combined-field representation (“CFIE”) is not needed here to prevent spurious resonances, as in the case of a bounded obstacle [16]. In fact (19) is sufficient when the unbounded  $\partial\Omega$  is a graph of a function, because then the Dirichlet BVP in the complementary domain  $\mathbb{R}^2 \setminus \overline{\Omega}$  is unique for any  $\omega$ ; see theorem 4 below and its proof.*

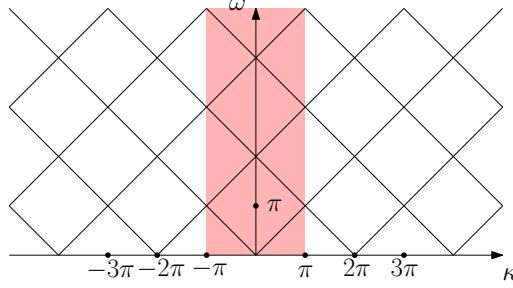


Figure 2: Location of Wood anomalies (black lines) and the first Brillouin zone (red shaded region of the  $\kappa$  axis) in the  $\omega$ - $\kappa$  plane, for the case of spatial periodicity  $d = 1$ .

### 2.1. Evaluation of quasiperiodic Green's functions

Here we describe an efficient numerical scheme to evaluate  $\Phi_p(\mathbf{x})$  appearing in the above BIE, using a local expansion about the origin, with lattice sum coefficients evaluated following [51]. Note that, since it is only valid up to a vertical height comparable to the unit cell width, a different plane-wave representation given in section 2.3 will be used for  $x_2$  values beyond this. Recall the definitions (5) and (6), and that a Wood anomaly is a point in the  $(\omega, \kappa)$  parameter plane where  $\kappa_n$  crosses  $\kappa_n = \omega$ . At such anomalies  $\Phi_p$  does not exist (e.g. see [49, 35]). We will thus assume that  $(\omega, \kappa)$  is not at a Wood anomaly (and direct the reader to [35, 36] for methods for quasiperiodic problems precisely at Wood anomalies).

The quasiperiodic Helmholtz Green's function in 2D is given by [49]

$$\Phi_p(x_1, x_2; \omega, d, \alpha_0) = \frac{i}{4} \sum_{n=-\infty}^{\infty} H_0^{(1)} \left( \omega \sqrt{(x_1 - nd)^2 + x_2^2} \right) \alpha^n. \quad (25)$$

The sum's slow, conditional convergence means it is of little practical use. We follow the approach described in [51] to rewrite it in terms of rapidly convergent lattice sums. Our derivation, however, differs in two key ways; we therefore reproduce some of the calculation below for convenience. Graf's addition theorem [58, (10.23.7)] is used first to expand each of the  $H_0^{(1)}$  centered on source point with an  $x_1$  coordinate outside of the unit cell,  $|x_1| > \frac{d}{2}$ , around the equivalent point inside the unit cell. The resulting expression contains the Bessel functions  $H_n^{(1)}$  and  $J_n$ . Terms multiplying the same-order  $J_n$  are collected; their coefficient, the  $n$ th order lattice sum  $S_n$ , is expressed as a contour integral. For faster convergence, following [35], we instead exclude  $|n| \leq 1$  from the sum in (25) and add them together directly; this can be thought of splitting the periodic Green's function into a near and far component:

$$\Phi_p = \Phi_{p,\text{near}} + \Phi_{p,\text{far}}, \quad (26)$$

with

$$\Phi_{p,\text{near}} = \frac{i}{4} \left[ H_0^{(1)}(\omega\rho_0) + \alpha^{-1} H_0^{(1)}(\omega\rho_1) + \alpha H_0^{(1)}(\omega\rho_{-1}) \right], \quad (27)$$

where  $\rho_j = \sqrt{(x_1 - jd)^2 + x_2^2}$ . We use Graf's theorem on the remaining terms to write

$$\Phi_{p,\text{far}} = \frac{i}{4} S_0(\omega d, \kappa) J_0(\omega\rho_0) + \frac{i}{2} \sum_{n=1}^{\infty} S_n(\omega d, \kappa) J_n(\omega\rho_0) \cos(n\phi), \quad (28)$$



where  $\phi$  is the angle describing the source-target displacement vector  $(x_1, x_2)$  in polar coordinates. The lattice sums  $S_n$  are independent of the source-target displacement, therefore they only need to be computed once for each value of  $\omega$  and  $\kappa$ . We follow [51] to derive the integral representation

$$S_n(\omega d, \kappa) \approx -ie^{i\frac{\pi}{4}} \frac{\sqrt{2}}{\pi} \left[ (-1)^n \alpha^{-2} \int_0^a [G_n(\tau) + G_n(-\tau)] F(\tau; \omega d, \kappa) d\tau + \alpha^2 \int_0^a [G_n(\tau) + G_n(-\tau)] F(\tau; \omega d, -\kappa) d\tau \right], \quad (29)$$

with  $\tau = (1 - i)t$  and

$$G_n(t) = \left( t - i\sqrt{1-t^2} \right)^n, \quad (30)$$

$$F(t; \omega d, \kappa) = \frac{e^{2i\omega d \sqrt{1-t^2}}}{\sqrt{1-t^2} [1 - e^{i\omega d (\sqrt{1-t^2} - \kappa/(\omega d))}]}. \quad (31)$$

The integrals appearing in  $S_n$  may be evaluated numerically using the trapezoidal rule. The reason behind (29) being an approximate expression instead of an equality is that upper limit of the integrals,  $a$ , has been truncated from  $\infty$ , exploiting the fact that the integrand decays quickly for  $t \gg 1$  due to the exponential factor in  $F$ .

Three convergence parameters are needed here: the number of terms  $N$  at which the sum in  $\Phi_{p,\text{far}}$  (in (28)) is truncated, the upper limit  $a$  of the integrals in (29), and the number of nodes  $M$  used in the trapezoidal rule to calculate (29). For the typical  $\omega$  and accuracies that we present, we found  $N = 40$ ,  $a = 15$ , and  $M = 10^4$  sufficient.

## 2.2. Discretizing the boundary integral

We discretize and solve the integral equation (24) using the Nyström method [38, Sec 12.2], summarized below. First, (24) is written in the standard form

$$\sigma(t) - \int_a^b K(t, s) \sigma(s) ds = f(t) \quad \text{for } t \in [a, b], \quad (32)$$

where  $K(t, s)$  is the appropriate kernel function, and the boundary is parameterized by  $s$  that runs from  $s = a$  to  $s = b$ . Then, the unknown *density* function  $\sigma(t)$  is approximated by another function  $\sigma_n(t)$  that obeys

$$\sigma_n(t) - \sum_{j=1}^n w_j K(t, s_j) \sigma_n(s_j) = f(t), \quad (33)$$

where the integral has been replaced with a quadrature formula with nodes  $\{s_i\}_{i=1}^n$  and weights  $\{w_i\}_{i=1}^n$ , and the kernel function  $K$  with a rank- $n$  operator. Then the values of  $\sigma_n(t)$  at the nodes  $\{s_i\}$ ,  $\{\sigma_i^{(n)}\} := \{\sigma_n(s_i)\}_{i=1}^n$  satisfy the linear system

$$\sigma_i^{(n)} - \sum_{j=1}^n w_j K(s_i, s_j) \sigma_j^{(n)} = f(s_i), \quad \forall i = 1, 2, \dots, n, \quad (34)$$

or in matrix notation,

$$A\sigma^{(n)} = \mathbf{f}, \quad (35)$$

with  $A_{ij} = \delta_{ij} - K(s_i, s_j)w_j$ . Then if any vector  $\sigma^{(n)} := \{\sigma_i^{(n)}\}$  solves the above system, then  $\sigma^{(n)}(t)$  at any  $t$  can be reconstructed as

$$\sigma^{(n)}(t) = f(t) + \sum_{j=1}^n w_j K(t, s_j) \sigma_j^{(n)}. \quad (36)$$

Substituting the kernel associated with our exterior Helmholtz problem with boundary  $\partial\Omega := z(s)$ , the  $A$  matrix in (35) becomes:

$$A_{ij} = \delta_{ij} - 2w_j z'(s_j) \frac{\partial \Phi_p(s_i, s_j)}{\partial \mathbf{n}_{s_i}}, \quad i, j = 1, 2, \dots, n, \quad (37)$$

while the components of  $\mathbf{f}$  are given by

$$f_j = 2(u_i)_n(s_j), \quad j = 1, 2, \dots, n. \quad (38)$$

Finally, the gradient of  $\Phi_p$ , necessary for filling the  $A$ -matrix in (37), is

$$\begin{aligned} \nabla \Phi_p(\mathbf{x}, \mathbf{y}) = & \frac{i}{4} \left( -\omega H_1^{(1)}(\omega\rho_0) \frac{\mathbf{x} - \mathbf{y}}{\rho_0} - \omega H_1^{(1)}(\omega\rho_1) \frac{\mathbf{x} - \mathbf{y} - d\mathbf{e}_{x_1}}{\rho_1} \right. \\ & \left. - \omega H_1^{(1)}(\omega\rho_{-1}) \frac{\mathbf{x} - \mathbf{y} + d\mathbf{e}_{x_1}}{\rho_{-1}} - \omega J_1(\omega\rho_0) S_0 \frac{\mathbf{x} - \mathbf{y}}{\rho_0} \right. \\ & \left. + 2 \sum_{n=1}^{\infty} \omega J_n'(\omega\rho_0) \cos(n\phi) S_n \frac{\mathbf{x} - \mathbf{y}}{\rho_0} + n J_n(\omega\rho_0) \sin(n\phi) S_n \frac{\hat{\mathbf{n}}_{\mathbf{x}-\mathbf{y}}}{\rho_0} \right), \end{aligned} \quad (39)$$

where  $\rho_j := \sqrt{(x_1 - y_1 - jd)^2 + (x_2 - y_2)^2}$ ,  $\hat{\mathbf{n}}_{\mathbf{x}-\mathbf{y}} := (x_2 - y_2, -(x_1 - y_1))/\rho_0$  is a unit normal to the displacement vector  $\mathbf{x} - \mathbf{y}$ , and  $\mathbf{e}_{x_1}$  is a unit vector in the  $x_1$  direction.

The key task for achieving high-order accuracy is in choosing the appropriate quadrature nodes and weights appearing in (33). For smooth boundaries, efficient quadrature rules are known, based on either the global periodic trapezoid rule, or high-order panel-wise quadrature. For boundaries with corners, however, the density function  $\sigma$  is singular at the corners. The closeness of this singularity limits the radius of the Bernstein ellipse associated with the interpolant used in Gaussian quadrature rules, which in turn degrades the accuracy of interpolation and quadrature [59, Ch 8, 19]. To maintain the order of accuracy whilst keeping the number of quadrature nodes the same, the size of the quadrature interval needs to be reduced as the corner is approached, *i.e.* the quadrature grid needs to be refined according to the features of the boundary [60]. We divide the two sides of unit cell boundary into equally-spaced panels, and use  $P$ -th order Gauss–Legendre nodes and weights on each, *i.e.*  $s_i$  and  $w_i$  are always the Gauss–Legendre nodes and weights on the standard interval  $[-1, 1]$ . Then for each panel with a corner as an endpoint, we divide the panel in a  $1 : (r - 1)$  ratio with  $r \geq 2$ , using the same  $P$ -th order Gauss–Legendre scheme on each. With  $r = 2$  (dyadic refinement), the net error after  $O(\log_2(1/\varepsilon))$  levels of refinement will be  $O(e^{-P} \log_2(1/\varepsilon))$ , where  $\varepsilon$  is a given numerical precision [60]. Moving from a single set of  $n$  global quadrature nodes to panel quadrature with  $Q$  panels, each with  $P$  nodes, modifies the expression (34) to

$$\sigma_{j,i} - \sum_{q=1}^Q \sum_{p=1}^P w_{j,i,q,p} K(s_{j,i}, s_{q,p}) \sigma_{q,p} = f_{j,i}, \quad j = 1, \dots, Q, \quad i = 1, \dots, P, \quad (40)$$

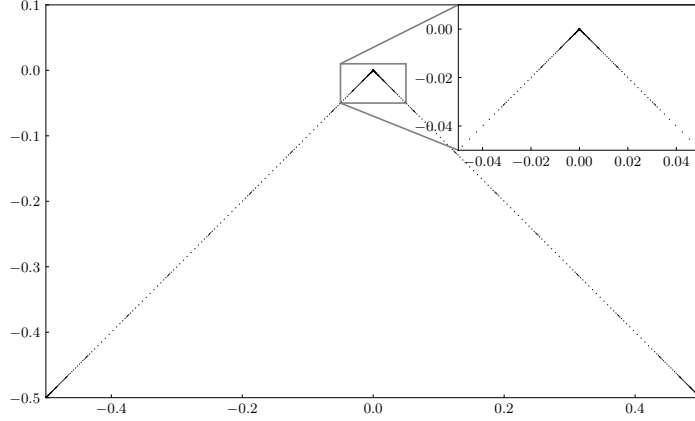


Figure 3: Discretization nodes on a single unit cell  $\Gamma$  of the boundary. The underlying coarse discretization has 8 equal panels on each straight line. Panels touching corners have then been subdivided dyadically 10 times, with shrinkage ratio  $r = 2$ . Each resulting panel was populated with 16 Gauss–Legendre quadrature nodes. An inset shows the result of the refinement.

where  $s_{ji}$  is the  $i$ -th Gauss–Legendre node on the  $j$ -th panel,  $\sigma_{ji}$ ,  $f_{ji}$ ,  $w_{ji}$  are the corresponding density, boundary data, and quadrature weights, and  $K(s_{ji}, s_{q,p})$  is the value of the kernel associated with the given pair of quadrature nodes.

Typically, different quadrature rules are needed depending on where  $s_{ji}$  and  $s_{q,p}$  (the “target” and “source” points) lie relative to each other [54, 61], with special care required if they lie on adjacent or the same panel. The need for this can be seen by inspecting (39) as  $\mathbf{x} \rightarrow \mathbf{y}$ : simple Gauss–Legendre rules cannot capture the (weak) singularity that emerges in this limit, therefore the close-to-diagonal entries in  $A$  will not be accurate. In the special case of the staircase, however, it is possible to achieve higher order accuracy without invoking special quadrature rules: since quadrature panels are straight lines, the interaction between source and target points on the same or colinear panels vanishes. This is clear from (37) and (39):  $\mathbf{x} - \mathbf{y}$  is perpendicular to  $\mathbf{n}_{\mathbf{x}}$  in this case.

Decrease in accuracy can arise from catastrophic cancellation if  $|\mathbf{x} - \mathbf{y}| \ll |\mathbf{x}|, |\mathbf{y}|$ , *e.g.* nodes lying on small panels either side of a corner. To mitigate this, we parameterize the quadrature panels such that the quadrature nodes’ positions are measured relative to the nearest corner.

Note that reconstructing the solution  $u_s$  close to the boundary would require special quadrature rules, since the position vectors of the target and source points are not necessarily colinear. Since such special rules are beyond the scope of this paper, the numerical solution will not be accurate within roughly the length of the nearest boundary panel. Fortunately this will not prevent us from extracting the trapped power to full accuracy.

### 2.3. Reconstructing the solution

Once the density evaluated at the boundary nodes,  $\sigma^{(n)}$ , is obtained, one may compute the scattered field  $u_s$  at a point  $\mathbf{x}$  inside the unit cell from its single-layer representation,

$$u_s(\mathbf{x}) = \sum_{j=1}^n w_j z'(s_j) \Phi_p(\mathbf{x}, s_j) \sigma_j^{(n)}. \quad (41)$$

(After which,  $u(t) = u_i(t) + u_s(t)$ .) The lattice sum representation of  $\Phi_p$ , and hence the above expression, quickly loses accuracy outside of the circle  $(x_1 + x_2)^2 = \frac{3d}{2}$  due to the application of Graf's addition theorem<sup>2</sup>.

Above the unit cell, the upwards propagating radiation condition may be exploited as follows. Let  $x_j := -\frac{d}{2} + \frac{jd}{N}$  for  $j = 0, 1, \dots, N-1$  and  $u_j^0 := u(x_j, x_2^0)$ . Evaluating the radiation condition at  $x_2 = x_2^0$ , notice that after rearranging, it takes the form of a discrete Fourier transform:

$$u_j^0 e^{-ikx_j} = \sum_{n \in \mathbb{Z}} \tilde{c}_n e^{i2\pi nx_j}, \quad (42)$$

with  $\tilde{c}_n = c_n e^{ik_n x_2^0}$ . Therefore, using the convention from [62, Ch. 12.1],

$$\tilde{c}_n = \frac{1}{N} \mathcal{F} \left( \{u_j^0 e^{-ikx_j}\}_{j=0}^{N-1} \right)_n, \quad (43)$$

and

$$u(x_j, x_2) = N \cdot \mathcal{F}^{-1} \left( \{\tilde{c}_n e^{i(k_n(x_2 - x_2^0) + ikx_j)}\}_{n=0}^{N-1} \right)_j. \quad (44)$$

In the  $n$ th neighboring unit cell, *i.e.*  $\frac{(2n-1)d}{2} < x_1 \leq \frac{(2n+1)d}{2}$  (at any given  $x_2$ ), the solution is found using the quasiperiodicity condition,

$$u(x_1 + nd, x_2) = \alpha^n u(x_1, x_2). \quad (45)$$

#### 2.4. Convergence check via flux conservation

In the absence of sources or sinks inside a closed boundary  $\Gamma$ , the net acoustic power (flux) leaving  $\Gamma$  is zero. How close it is to zero numerically can be used to measure the accuracy of the method and investigate convergence in terms of the size of the linear system (35). The acoustic power passing through a surface is<sup>3</sup>

$$F_\Gamma = \text{Im} \left( \int_\Gamma \bar{u} u_n ds \right). \quad (46)$$

To test the convergence of the method above, we choose the incident wave to be a plane wave,  $u_i = e^{i\omega \mathbf{n}_i \cdot \mathbf{x}}$ , where  $\mathbf{n}_i$  is a unit vector describing its direction of travel. This corresponds to the limit of moving a quasiperiodic point source array to infinity in the vertical direction. Specifically,  $\mathbf{n}_i = (\cos(\phi_i), \sin(\phi_i))$  with  $-\pi \leq \phi_i \leq 0$ . Then  $\kappa = \omega \cos(\phi_i)$ . Let  $\Gamma$  be the perimeter of the unit cell as shown in fig. 1, bounded from below by the stair boundary, above by the line  $x_2 = \frac{d}{2}$ , and from the two sides by  $x_1 = \pm \frac{d}{2}$ . The net flux through the two sides has to be zero by symmetry, and it is also zero across the lower edge of  $\Gamma$  due to Neumann boundary conditions. Therefore we have

$$F_\Gamma = \text{Im} \left( \int_{-d/2}^{d/2} \bar{u} \frac{\partial u}{\partial x_2} dx_1 \right) = 0. \quad (47)$$

In fig. 4 we evaluate  $F_\Gamma$  as we refine the corner-adjacent panels with  $r = 3$ . Initially there are  $Q = 8$  panels on each side with  $P = 8$  nodes on each, and after  $R$  levels of refinement, there are

<sup>2</sup>This would be a smaller, radius- $\frac{d}{2}$  circle were  $n = \pm 1$  not excluded from (28).

<sup>3</sup>See [10], or follow the derivation in [19]: start from (95), then substitute in (92), the 3D generalization of (82), and use harmonicity.

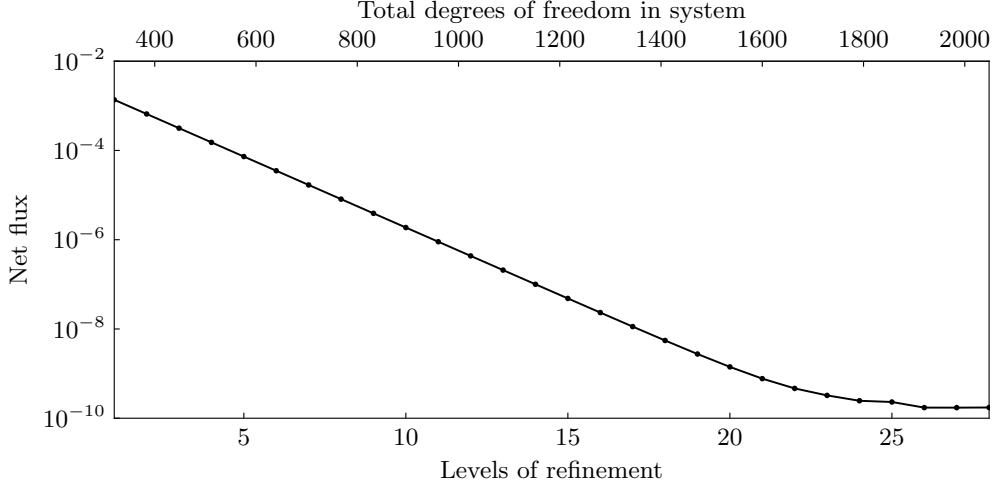


Figure 4: Convergence test via flux conservation for the case of an incident plane wave. The figure shows the net flux exiting the central unit cell, which is analytically zero, as a function of both the number of times the corner-adjacent quadrature panel has been subdivided on the boundary, and the size of the resulting linear system. During refinement the panels have been split in a 1 : 2 ratio ( $r = 3$ ).

$Q = 2(8 + 2R)$  panels and a total of  $PQ = 128 + 32R$  nodes. The experiment used  $\omega = 4.0$ , and  $\phi_i = -0.5$ . The figure confirms exponential convergence and suggests that around 10 levels of refinement are needed for  $\approx 7$  digits of accuracy, and around 22 for 10 digits, at which point the system size is still smaller than  $10^3 \times 10^3$ . The reduction of error stops at this point, which is roughly consistent with the spacing between the closest quadrature nodes approaching machine precision.

### 3. Trapped acoustic modes and the raindrop effect

In this section we describe and test a Fredholm determinant method to find evanescent modes trapped by the corrugated sound-hard interface. Such modes are eigenfunctions, i.e., nontrivial solutions to the homogeneous quasiperiodic BVP (7) to (10), for some  $\kappa \in \mathbb{R}$  and  $\omega > 0$ . Their parameters form a continuous families, thus curves in the  $(\omega, \kappa)$  plane, known as the *band structure* [2, 10]. Each curve may be described by its trapped mode frequency  $\omega_{\text{tr}}(\kappa)$ , commonly referred to as a dispersion relation. For staircase geometries we find empirically that there is only a single such trapped frequency at each wavenumber  $0 < |\kappa| \leq d/2$  in the Brillouin zone, as shown in fig. 5.

Recall that the quasiperiodic BVP has the BIE formulation (24). With homogeneous boundary data this becomes the BIE

$$(I - 2D^T)\sigma = 0, \quad (48)$$

with  $D^T$  the adjoint double-layer operator from the previous section. One might then hope that the condition for a trapped mode to exist is equivalent to the existence of a nontrivial density  $\sigma$  solving (48). We now show that this is indeed so, thus that the proposed numerical method is robust (free of spurious resonances).

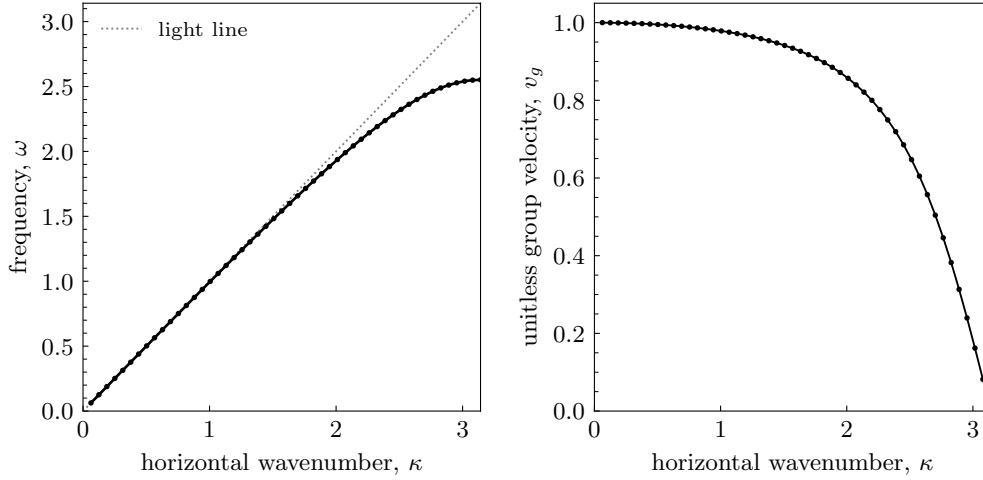


Figure 5: Left: numerically computed band structure (dispersion relation) for evanescent trapped modes of the  $\pi/4$ -slope staircase with period  $d = 1$ . Only the right (positive) half of the Brillouin zone is shown. Dots show the band structure  $\omega_r(\kappa)$ , and the line shows the values  $\omega = \kappa$ . Radiation into the upper half plane is only possible when  $\omega > |\kappa|$ . Right: group velocity  $v_g := d\omega_r(\kappa)/d\kappa$  plotted over the same domain.

**Theorem 4.** Fix  $\omega > 0$  and  $\kappa \in \mathbb{R}$ . There is a trapped mode (i.e., a nontrivial  $\phi$  solving the homogeneous quasiperiodic BVP (7) to (10)) if and only if  $\dim \text{Nul}(I - 2D^T) > 0$ .

*Proof.* Let  $\sigma$  be a nontrivial solution to  $(D^T - I/2)\sigma = 0$ , and let  $\phi = \mathcal{S}\sigma$  throughout  $\mathbb{R}^2$ , recalling that  $\mathcal{S}$  is the quasiperiodic single-layer potential on  $\Gamma$  (the part of  $\partial\Omega$  in the central unit cell). Then  $(\Delta + \omega^2)\phi = 0$  in  $\mathbb{R}^2 \setminus \partial\Omega$ . By the jump relations,  $\phi_n^+ = 0$  (using the notations (20) and (21)), and by construction  $\phi$  also satisfies (9) and (10). It remains to show that  $\phi$  is nontrivial. Assume this were so, then  $\phi^+ = 0$ , so by the jump relations,  $\phi^- = 0$ . However,  $\phi$  in the half-space below  $\partial\Omega$  would then be a homogeneous solution to the (downward-facing) quasiperiodic Dirichlet problem, which is unique [44, p. 56] [63, Thm. 2.1]. Thus  $\phi$  would vanish below  $\partial\Omega$ , so  $\phi_n^- = 0$ . By the jump relation  $\sigma = \phi_n^- - \phi_n^+$  would vanish, a contradiction with the hypothesis. Thus  $\phi$  is nontrivial, hence a trapped mode.

For the converse, let  $\phi$  be a trapped mode, then by the quasiperiodic version of Green's representation theorem, in the upper domain  $\phi = \mathcal{S}\phi_n^+ + \mathcal{D}\phi^+$ , where  $\mathcal{D}$  is the quasiperiodic double-layer potential defined by

$$(\mathcal{D}\sigma)(\mathbf{x}) := \int_{\Gamma} \frac{\partial \Phi_p(\mathbf{x}, \mathbf{y})}{\partial \mathbf{n}_y} \sigma(\mathbf{y}) ds_y.$$

Since  $\phi_n^+ = 0$ , and taking  $\mathbf{x}$  to  $\partial\Omega$  from above,  $\phi^+ = (D + I/2)\phi^+$ , showing that  $D - I/2$  has a nontrivial null vector. By the Fredholm–Riesz theory, the same holds for  $D^T - I/2$ , since it is the adjoint with respect to the bilinear form  $\langle \psi, \phi \rangle := \int_{\Gamma} \psi \phi ds$  [18].  $\square$

This informs our numerical approach: we fix  $\kappa$  and solve a nonlinear eigenvalue problem with respect to  $\omega$ . We adapt the Fredholm determinant method of Zhao and the 2nd author [57].

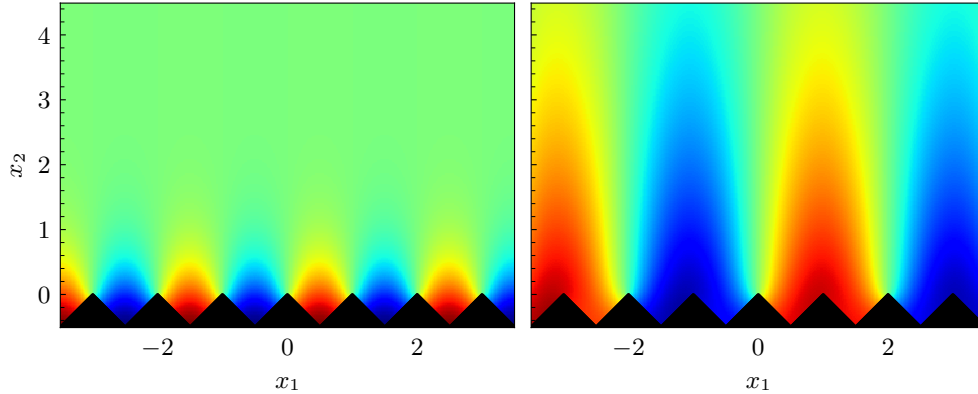


Figure 6: The real part of two example trapped modes  $\phi$ , for the  $\pi/4$  staircase with  $d = 1$ . Left: the highest frequency mode, at  $\kappa = \pi$ . Right: An intermediate frequency mode, at  $\kappa = 1.54$ .

$g(\omega) := \det(I - 2D^T)$  is approximated by an  $N \times N$  determinant, where  $I - 2D^T$  is replaced by its Nyström matrix with entries given by (37). At each  $\kappa$ , then  $\omega_{\text{tr}}(\kappa)$  is found as a root of  $g(\omega)$ , using a simple Newton iteration with a convergence criterion close to machine accuracy. For staircase geometries, we find only one such root, and always with  $\omega_{\text{tr}}(\kappa) < |\kappa|$ , implying that the mode is trapped (frequency is below the light line), rather than embedded in the continuous spectrum [2, 10]. Because the trapped frequencies never intersect the light lines, the issue of Wood anomalies does not cause a problem in the mode-finding task.

Figure 5 shows this set of  $\omega_{\text{tr}}$  found at each  $\kappa$ . The gap between  $\omega_{\text{tr}}(\kappa)$  and  $|\kappa|$  indicates the strength of trapping (rapidity of evanescent decay as  $x_2 \rightarrow \infty$ ). The most trapped mode is at  $\kappa = \pm\pi$ , known as an “optical mode”, and has  $\omega_{\text{tr}} \approx 2.551$  for the  $d = 1$  staircase. As  $\kappa \rightarrow 0$  we see trapping becoming arbitrarily weak.

With a zero of the determinant found, the null vector  $\sigma$  obeying  $(I - 2D^T)\sigma = 0$  is found via an SVD, then  $\phi = S\sigma$  gives the mode. Numerically the lattice-sum expansion may only be used up to a height around  $d/2$  above the origin, so as before one must switch to Fourier series evaluation above this. Figure 6 shows the real part of example modes.

### 3.1. Ray model for time-domain chirp response at El Castillo

The above trapped mode dispersion curve provides a simple explanation of the acoustic “rain-drop” effect on the long stone staircases at the *El Castillo* pyramid at Chichen-Itza.<sup>4</sup> Impulsive sources of sound, such as footsteps, are reported to sound like short chirps (frequency rising vs time) when heard from distances far up or down the staircase. Pending a full numerical investigation of the time-domain solution to (1) and (2), we use a simple ray model for dispersive propagation [64, Sec. 2.6]. Both source and receiver are assumed to be close enough to the surface to couple well to the modes  $\phi$  at all wavenumbers (this is true for a footstep, less obviously so for a standing listener). Absorption and modeling of amplitudes are ignored. Impulsive excitation in (1) is assumed to excite all frequencies. Each frequency  $\omega$  below the maximum of  $\omega_{\text{tr}}$

<sup>4</sup>We are very grateful to Eric Heller for suggesting this explanation; it is also described by Heller in [15, p. 162].

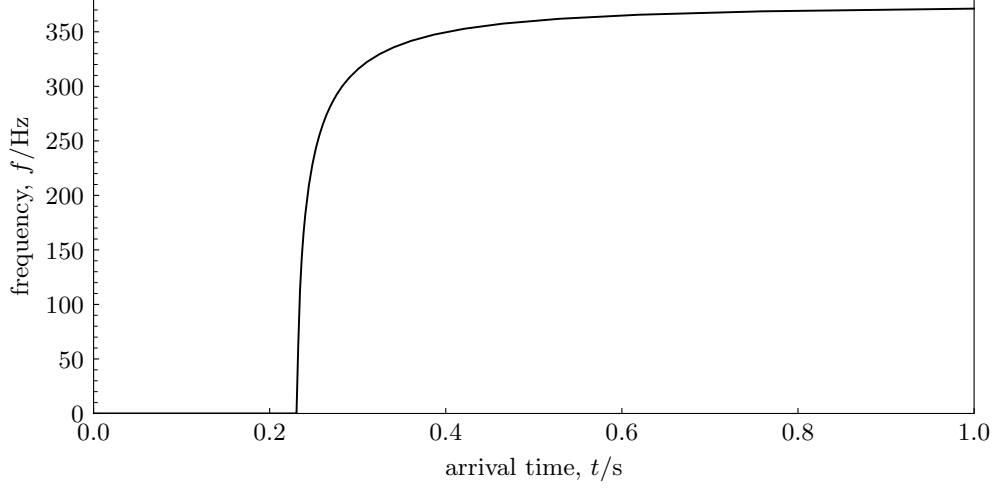


Figure 7: Graph of frequency (in Hz) vs time (in seconds since emission) observed a distance  $D$  along a sound-hard staircase from an impulsive source for the wave equation. Parameters for the *El Castillo* staircase are used, with  $D$  the full 91 steps comprising one side of the pyramid.

is partly trapped (see section 5), and this component propagates along the staircase at its *group velocity*

$$v_g = \frac{d\omega_{\text{tr}}}{d\kappa}, \quad (49)$$

at the appropriate  $\kappa := \kappa_{\text{tr}}$  such that  $\omega_{\text{tr}}(\kappa) = \omega$ . We plot  $v_g$  vs  $\kappa$  on the right of fig. 5, by differentiating the interpolant of  $\omega_{\text{tr}}$  on the  $\kappa$ -grid. The frequency's arrival time a distance  $D$  along the staircase is thus  $t(\omega) = D/v_g(\omega)$ . Finally, inverting this last relationship gives the frequency  $\omega$  heard at each time  $t$  after the impulse.

We now insert physical parameters for *El Castillo*. The nondimensionalized speeds used in the rest of the paper must be multiplied the sound speed  $c = 343$  m/s. According to [65] the stairs at this pyramid have depth equal to height equal at  $q = 0.263$  m, i.e. a  $\pi/4$  staircase with period  $d = \sqrt{2}q \approx 0.372$  m. The maximum trapped mode frequency is thus  $(c/d)2.551 \approx 374$  Hz; this is the highest frequency explainable in the model.<sup>5</sup> Each staircase has 91 steps, giving  $D \approx 34$  m.

The resulting predicted frequency vs arrival time is shown in fig. 7. The first arrivals are the lowest frequencies; for these the dispersion curve is almost that of free air ( $v_g \approx c$ ) so they start arriving immediately after any direct (non-trapped) radiation. Most of the frequency “chirp” occurs during the first 0.2 s after first arrival, an interval containing of order 50 cycles, and thus plenty to detect the upwards frequency trend. A long “bell-like” tail, asymptoting to the maximum 374 Hz, is expected, associated with the slowly-propagating optical modes as shown on the left of fig. 6.

<sup>5</sup>The frequency of a free-space plane wave traveling along the staircase with wavenumber at the Brillouin zone edge  $\kappa = \pi/d$  is  $c/2d \approx 461$  Hz. Neither of these frequencies appear in [14], although a “raindrop frequency” of 307.8 Hz is mentioned.



**Remark 5.** We provide a link to a WAV file simulated to match the above chirp prediction at this URL: <https://doi.org/10.5281/zenodo.10005461>. The authors do not have access to audio recordings of footsteps on this staircase, and would welcome the chance to validate the predictions.

#### 4. Scattering from a single point source

As laid out in section 1, we simulate scattering from a single point source by integrating over the solutions from a quasiperiodic array of point sources with different  $\kappa$  values. Let  $u_{\kappa,i}(\mathbf{x}) = \Phi_{p,\kappa}(\mathbf{x}, \mathbf{x}_0)$ , where the subscript  $\kappa$  refers to having fixed  $\kappa$  and  $x_0$  is a given source position within the central unit cell. Then from (11) and (12) it follows that

$$u_i(\mathbf{x}) = \Phi(\mathbf{x}, \mathbf{x}_0) = \frac{1}{2\pi} \int_{-\pi}^{\pi} u_{\kappa,i}(\mathbf{x}) d\kappa, \quad (50)$$

and, with  $u_{\kappa}(\mathbf{x})$  referring to the total field due to the above incident field  $u_{\kappa,i}(\mathbf{x})$ , the array scanning integral is

$$u(\mathbf{x}) = \frac{1}{2\pi} \int_{-\pi}^{\pi} u_{\kappa}(\mathbf{x}) d\kappa = \frac{1}{2\pi} \int_{-\pi}^{\pi} (u_{\kappa,i}(\mathbf{x}) + u_{\kappa,s}(\mathbf{x})) d\kappa, \quad (51)$$

where  $u_{\kappa,s}$  is the scattered field associated with  $u_{\kappa,i}$ .

To achieve high-order accuracy one must understand the complex  $\kappa$  plane singularities of the above integrand. For example, in fig. 8 we plot the integrand in (51) for a target point  $\mathbf{x} = (0.22, -0.16)$ , frequency  $\omega = 2.4$ , and source point  $x_0 = (-0.2, 0.1)$ . Each side of the stair boundary was split into 4 panels initially, then refined 5 times with  $r = 3$ , until the total number of quadrature panels over the boundary was  $Q = 28$ , each with  $P = 16$  nodes. This gives around 7 accurate digits according to the convergence test in fig. 4. The two key features in the figure are the branch points due to Wood anomalies at  $\kappa = \pm\omega$ , and two poles at  $\kappa = \pm\kappa_{\text{tr}}$ . They are ordered such that  $\omega \leq \kappa_{\text{tr}} \leq \pi$ . The branch cuts associated with the branch points are indicated by dashed lines. The direction of the branch cuts can be chosen by altering the integration path in (29) (by choosing  $\tau(t)$ ), but as it will become clear later, it is convenient to choose the cuts to lie in the lower and upper half-plane for negative and positive  $\kappa$ , respectively. If  $\omega$  were larger than  $\omega_c$ , where no trapped modes exist for any  $\kappa$ , there would be no poles. In the limits  $\omega \rightarrow 0$  and  $\omega \rightarrow \omega_c$ , the two poles coalesce at  $\kappa_{\text{tr}} \rightarrow 0$  and  $\kappa_{\text{tr}} \rightarrow \pm\pi$  respectively.

The branch points and poles in (51) require careful treatment. If  $\omega > \omega_c$ , the branch points can be integrated over without leaving the real axis, due to Wood anomalies being known to be square-root singularities [31, 32, 66, 67]. They may then be dealt with using special Gaussian quadrature, e.g. [68]. With the emergence of the trapped mode poles at  $\omega \leq \omega_c$ , options include singularity extraction [20], and contour deformation [7, 69]. We opt for the latter, deforming the contour away from the real axis and the branch cuts, as shown by the solid black line in fig. 8.

Note that in order for the solution to correspond to outgoing waves, the integration contour has to be deformed into the upper half-plane for negative  $\kappa$  and the lower half-plane for positive  $\kappa$ . This idea was introduced in [70] and termed the *limiting absorption principle* by [71]. The direction of the branch cuts was chosen with this in mind, following [23].

We choose a sinusoidal deformation contour parameterized by  $k := \text{Re } \kappa$ ,

$$\kappa(k) = k - iA \sin(k), \quad (52)$$

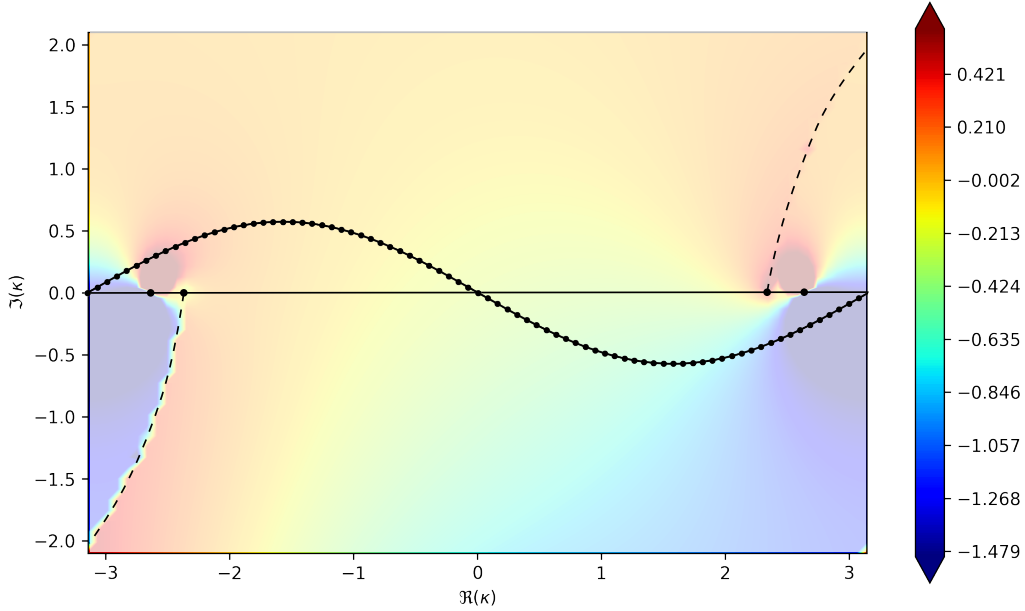


Figure 8: Real part of the integrand of the array scanning integral (51) plotted in the complex  $\kappa$ -plane, where the field is evaluated at a single target,  $\mathbf{x} = (0.22, -0.16)$ . Plotted over this are the branch points and cuts (dots with dotted lines), poles (dots), and the contour deformation used (solid black line, with an example set of 80 quadrature nodes plotted on top).

which is then discretized using the periodic trapezoidal rule with  $p_{\text{asm}}$  nodes. To get an idea of what accuracy a given  $A$  and  $p_{\text{asm}}$  yields, we use (50) as a test problem, and investigate how accurately  $\Phi$  can be reconstructed from  $\Phi_{p,\kappa}$  in fig. 9. The top part of the figure shows the real part of total solution  $u(\mathbf{x})$ , computed to 7 digits of accuracy at  $\omega = 2.4$ , with a point source at  $\mathbf{x}_0 = (-0.2, 0.1)$ . The bottom part of fig. 9 shows that the exponential convergence rate is sensitive to the exact value of the amplitude, and that values between 0.5 and 2 are optimal. In this range,  $p_{\text{asm}} \approx 100$  quadrature nodes are enough to get an answer accurate to machine precision.

So far we only considered computation of the solution inside the central unit cell (and above it),  $-\frac{d}{2} \leq x_1 \leq \frac{d}{2}$ . Using the quasiperiodicity property, the array scanning integral (51) for a target position in the  $n$ th unit cell becomes

$$u^n(\mathbf{x}) := u(x_1 + nd, x_2) = \frac{1}{2\pi} \int_{-\pi}^{\pi} u_{\kappa}(\mathbf{x}) e^{ind\kappa} d\kappa. \quad (53)$$

Figure 10 shows the array scanning integrand at a target  $n = 5$  unit cells away from the center, to be compared to fig. 8. The exponential factor causes oscillations in the real and exponential growth in the imaginary direction in the lower (upper) half-plane for positive (negative)  $n$ . The

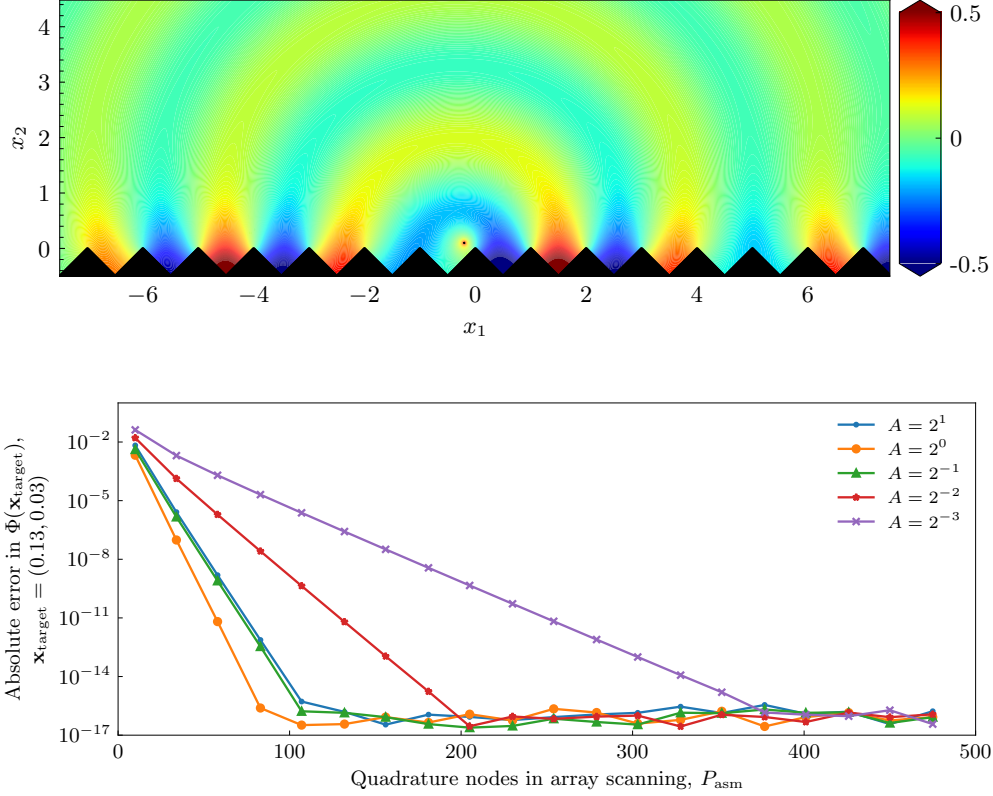


Figure 9: Top: Real part of total acoustic pressure field from a point source at  $\mathbf{x}_0 = (-0.2, 0.1)$ , radiating with frequency  $\omega = 2.4$ , accurate to 7 digits. Bottom: convergence test of the reconstruction of  $\Phi(\mathbf{x}_{\text{target}})$ , at  $\mathbf{x}_{\text{target}} = (0.13, 0.03)$ , with the array scanning method. The sinusoidal contour shown in fig. 8 was taken, with various amplitudes  $A$ , and discretized with  $p_{\text{asm}}$  trapezoidal quadrature nodes.

exponential growth limits the amount of contour deformation away from the real axis, and both the growth and oscillations demand more quadrature points to maintain constant accuracy as  $n$  increases. Thus as  $n$  grows, quadrature along the contour becomes a less practical method to evaluate the solution.

However, in the limit  $n \rightarrow \pm\infty$ , the solution may be computed easily in a different manner. Consider first the case  $n \rightarrow +\infty$ . We deform the sinusoidal contour to the contour shown in orange in fig. 10; if there is a trapped mode (pole) at  $\kappa_{\text{tr}}$  then this deformation introduces a correction by the residue of that pole. The contribution of the orange contour vanishes in the limit  $n \rightarrow +\infty$  by standard Jordan's lemma type arguments. Namely, the term  $e^{ind\kappa}$  vanishes for any  $\text{Im}\kappa > 0$ , making the contributions of the segments parallel to the branch cut, and the horizontal segments, zero. The other vertical segments cancel by periodicity. Taking the radius of the "keyhole" around the branch point to zero, its contribution vanishes since the integrand involves powers of at least  $-1/2$ . By Cauchy's theorem, the value of the array scanning integral is thus only the residue at  $\kappa_{\text{tr}}$ , if such a pole exists, and zero otherwise. Considering now only the case with such a residue, since the phase of  $u$  changes with  $n$ , one has to take care incorporating

the correct phase in order for a limit to exist:

$$\begin{aligned} u^{+, \infty}(x_1, x_2) &:= \lim_{n \rightarrow \infty} e^{-ind\kappa_{\text{tr}}} u(x_1 + nd, x_2) = \lim_{n \rightarrow \infty} \frac{1}{2\pi} \int_{-\pi}^{\pi} u_{\kappa}(x_1, x_2) e^{in(\kappa - \kappa_{\text{tr}})d} d\kappa \\ &= i \operatorname{Res}_{\kappa = \kappa_{\text{tr}}} u_{\kappa, s}(x_1, x_2). \end{aligned} \quad (54)$$

In the case  $n \rightarrow -\infty$ , we deform the sinusoidal contour into the lower half-plane, as shown in blue in fig. 10. By the same arguments, if a trapped mode exists, the solution is

$$u^{-, \infty}(x_1, x_2) := \lim_{n \rightarrow -\infty} e^{-ind\kappa_{\text{tr}}} u(x_1 + nd, x_2) = -i \operatorname{Res}_{\kappa = -\kappa_{\text{tr}}} u_{\kappa, s}(x_1, x_2), \quad (55)$$

and zero otherwise.

Finally, we explain how we numerically extract the residue at  $\kappa = \pm\kappa_{\text{tr}}$ , which can be viewed as extracting the left- and right-going trapped mode amplitudes. We use Cauchy's theorem once more, and integrate on a circular contour enclosing the relevant pole, applying a trapezoidal rule with  $p_{\text{res}}$  nodes. The radius of this circle,  $r_{\text{res}}$ , is chosen so that the amplitude of the integrand along the contour stays as close to 1 as possible, thus avoiding loss of accuracy due to catastrophic cancellation. The contour also needs to lie on one sheet, and therefore cannot cross a branch cut. The radius  $r_{\text{res}}$  is therefore determined by the distance to the nearest branch point or the distance to the nearest pole, whichever is smaller. We discuss the  $\kappa = +\kappa_{\text{tr}}$  case and use the same parameters for negative  $\kappa$ . By inspection of the dispersion relation in fig. 5, it is clear that for all but  $\kappa_{\text{tr}} \rightarrow \pi$ , the distance to the nearest branch point, at  $\kappa = \omega$ , is smaller. We use

$$r_{\text{res}} = \min(0.5 \cdot |\kappa_{\text{tr}} - \omega|, |\pi - \kappa_{\text{tr}}|) \quad (56)$$

to determine the radius, and  $p_{\text{res}} = 64$  nodes, after convergence testing by doubling  $p_{\text{res}}$ .

The main claim of the previous section is a direct consequence of the above result: at  $\omega < \omega_c$  the only contributor to the field infinitely far away from the source is the trapped mode at the given  $\omega$ . At  $\omega > \omega_c$ , where no trapped modes exist, the field in this limit is zero, since the contour in the complex  $\kappa$  plane contains no poles. As we have seen in section 3, trapped modes at different frequencies have different vertical decay lengths, and propagate at different speeds. It is therefore of interest to compute how much of the power injected into the system is transported away in trapped modes, as opposed to radiated vertically, as a function of frequency—this is the subject of the next section.

## 5. Extracting the asymptotically trapped power

In this section we find the total power injected into the system by a single point source, and compute the fractional power carried to infinity in trapped modes, as a function of frequency. The source  $\mathbf{x}_0$  is assumed to be inside the central unit cell, *i.e.*,  $-\frac{d}{2} < x_1^0 < \frac{d}{2}$ .

The total power radiated by a single point source can be derived by taking the total flux (46) exiting a circle of radius  $r$  (denoted  $\Gamma_r$ ), centered on the source, and then taking the limit  $r \rightarrow 0$ :

$$P_{\text{tot}} = \lim_{r \rightarrow 0} \left( \operatorname{Im} \int_{\Gamma_r} (\bar{u}_s + \bar{u}_i) \partial_n (u_s + u_i) ds \right). \quad (57)$$

Out of the four terms, only two contribute: since  $u_s$  and its derivative is finite everywhere, the integral of  $u_s \partial_n u_s$  vanishes; and  $u_i$  only grows like  $\ln r$  as  $r \rightarrow 0$ , therefore its contribution is

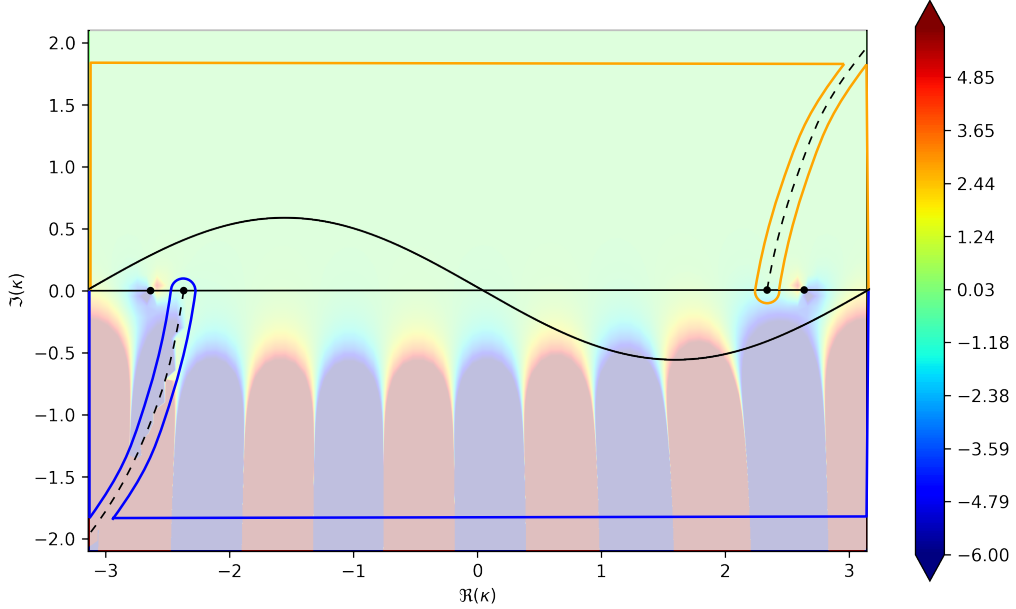


Figure 10: Real part of the array scanning integrand (53) with the target point  $n = 5$  unit cells away from the source, to be compared with fig. 8. Identical branch cuts, poles, and contour deformation are shown in black. In orange and blue we plot the contours we use to derive the field in the limit of  $n \rightarrow \pm\infty$ , respectively.

$\lim_{r \rightarrow 0} r \ln r = 0$ . Using the asymptotic form of  $H_0^{(1)}(\omega r)$  as  $r \rightarrow 0$  [58, Ch. 10.7], it can be shown that the remaining terms add up to

$$P_{\text{tot}} = \frac{1}{4} + \text{Im}(u_s(\mathbf{x}_0)). \quad (58)$$

Thus the radiated power is influenced by the scattered wave at the emission point.

For each value of  $\omega$ , we use the strategy outlined in section 4 to compute  $u_s(\mathbf{x}_0)$ , *i.e.* integrate along a deformed array scanning contour in  $\kappa$  using the trapezoidal rule. However, in the limits  $\omega \rightarrow 0$  (where  $\kappa_{\text{tr}} \rightarrow 0$ ), or  $\omega \rightarrow \omega_c$  (the cutoff frequency, where  $\kappa_{\text{tr}} \rightarrow \pi$ ), the contour must pass between two coalescing poles. This necessitates an increase in quadrature node density in the section of the contour closest to the poles. In these limits, it is therefore inefficient to evenly space the nodes in  $\text{Re } \kappa$ . We instead follow [72, Sec. 3] and define an exponentially graded reparameterization of the real part of  $\kappa$ , via a periodic map  $\theta : [-\pi, \pi) \rightarrow [-\pi, \pi)$ , namely

$$\kappa(k) = \theta(k) - iA \sin(\theta(k)), \quad \text{where } \theta'(k) = \begin{cases} \alpha \cosh\left(b \sin \frac{k}{2}\right) & \text{if } \kappa_{\text{tr}} \rightarrow \pi, \\ \alpha \cosh\left(b \sin \frac{k-\pi}{2}\right) & \text{if } \kappa_{\text{tr}} \rightarrow 0, \end{cases} \quad (59)$$

which bunches quadrature nodes that are evenly spaced in  $k$  by a factor of order  $e^b$  close to either  $\pi$  or 0. The normalization  $\alpha$  is determined numerically by requiring  $\int_0^{2\pi} \theta'(k) dk = 2\pi$ . To

Parameter	Description	Value
$A$	Amplitude of sinusoidal array scanning contour in (59)	1.0
$p_{\text{asm}}$	Number of trapezoidal nodes along sinusoidal array scanning contour	60
$b$	Exponential grading parameter along sinusoidal array scanning contour	0.0 if $0.5 \lesssim \omega \lesssim 2.6$ , 5.0 otherwise
$r_{\text{res}}$	Radius of circular contour for residual calculation	given by (56)
$p_{\text{res}}$	Number of trapezoidal nodes along circular residual contour	64
$\epsilon$	Tolerance for determining the upper limit (61) of trapped power integral (60)	$10^{-8}$
$p_{\text{tr}}$	Number of Gauss–Legendre nodes in trapped power integral (60)	128

Table 1: Parameters used in computing the fractional power transported by trapped modes, chosen so that the total power  $P_{\text{tot}}$  and power in trapped modes  $P_{\text{tr}}^{\pm}$  is accurate to 8 digits for all  $\kappa_{\text{tr}}$  considered, *i.e.*,  $\kappa_{\text{tr}}, \kappa_{\text{tr}} - \pi > 0.05$ .

achieve uniform accuracy as  $\kappa_{\text{tr}} \rightarrow 0$  or  $\kappa_{\text{tr}} \rightarrow \pi$ , one needs to update  $b$  as  $b = c_1 + c_1 \log \kappa_{\text{tr}}$  and  $b = c_3 + c_2 \log(\pi - \kappa_{\text{tr}})$ , respectively, where  $c_1$ – $c_3$  are constants to be determined. Here, we consider  $\kappa_{\text{tr}}, \pi - \kappa_{\text{tr}} > 0.05$ , for which we find (by doubling  $p_{\text{asm}}$  to gain an upper bound on the error) that setting  $b = 5$ ,  $p_{\text{asm}} = 60$  is sufficient to obtain a value for  $P_{\text{tot}}$  accurate to 8 digits. We therefore use these settings if  $\omega \lesssim 0.5$  or  $2.6 \lesssim \omega$ , and  $b = 0$  (evenly spaced nodes in  $\text{Re } \kappa$ ) otherwise. This parameter combination ensures that the nearest pole is at least 5 quadrature node spacing’s distance away from the contour.

As shown in section 4, the only contributors to the field infinitely far away from the source along the surface are trapped modes. Let  $\Gamma_{\infty}$  be the semi-infinite vertical line segment with a given  $x_1$  coordinate, starting on the surface. We can use (54) to reconstruct  $u^{+\infty}$  or  $u^{-\infty}$  on this line segment. Then the power in the left-going (–) or right-going (+) trapped modes is

$$P_{\text{tr}}^{\pm} = \pm \text{Im} \left( \int_{\Gamma_{\infty}} \bar{u}^{\pm, \infty} \partial_{x_1} u^{\pm, \infty} ds \right). \quad (60)$$

Note that this expression must be independent of the choice of horizontal position  $x_1$ , by power conservation. Furthermore, the phase introduced in (54) cancels. Given any  $x_1$ , we approximate (60) by a quadrature rule from the surface point  $x_2^0$  to an upper limit  $x_2^1$ , chosen such that the given trapped mode has sufficiently decayed. Based on the vertical mode intensity decay rate (twice the amplitude decay rate in (6)) we thus set  $x_2^1$  to

$$x_2^1(\kappa) := x_2^0 + \frac{\log(1/\epsilon)}{2\sqrt{\kappa^2 - \omega^2}}, \quad (61)$$

where  $\epsilon > 0$  is a desired error tolerance.

While the choice of  $x_1$  is immaterial mathematically, one choice is much more convenient numerically: the corner (trough) at  $x_1 = \pm \frac{d}{2}$  is best, for the following reason. Firstly,  $x_1$  passing through a corner is to be preferred to any other part of  $\Gamma$ , since the panels discretizing  $\Gamma$  are already geometrically refined towards corners, allowing accurate evaluation arbitrarily close to the corner via plain quadratures. (In contrast, were  $x_1$  to intersect any flat part of  $\Gamma$ , a special close-evaluation quadrature would be needed at points closer than one panel-size from  $\Gamma$ .) Secondly, to decide whether the upper ( $3\pi/2$  angle at  $x_1 = 0$ ) or lower ( $\pi/2$  angle at  $x_1 = \pm d/2$ ) corner is to be preferred, one expands the total field in terms of Bessel functions around either point and imposes Neumann boundary conditions. This shows that only the lower corner has a regular (hence analytic) expansion involving even powers. The potential at the upper corner is nonanalytic since it involves powers that are multiples of  $2/3$ . The above then implies that

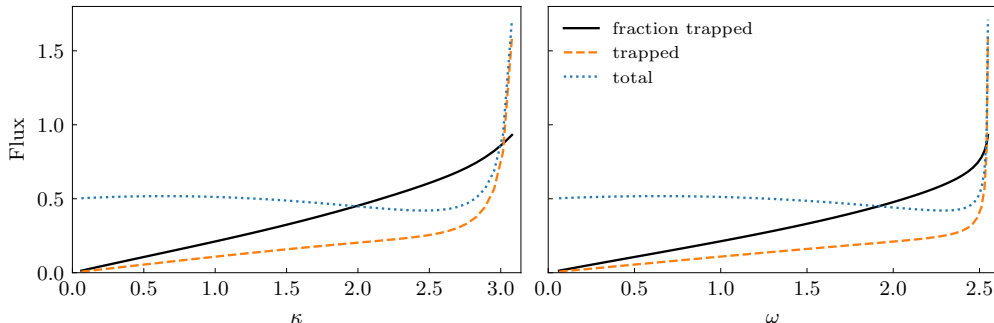


Figure 11: Left: Total flux (unitless) in the system, flux in trapped modes, and fraction of flux in trapped modes, as a function of Bloch wavenumber  $\kappa$ . Right: The same quantities plotted against the frequency  $\omega$  of the Helmholtz equation.

Gauss–Legendre quadrature with  $p_{\text{tr}}$  nodes is high-order accurate for the integral (60) along the line  $x_1 = \pm d/2$ , so this is what we use, with  $p_{\text{tr}} = 128$ .

Figure 11 shows the power balance as a function of  $\kappa$  on the left and  $\omega$  on the right, with power tolerance  $\epsilon = 10^{-8}$ . For reproducibility, we summarize the parameters used in table 1. Since the fluxes calculated here are unitless, we show the flux in trapped modes  $P_{\text{tr}}^+ + P_{\text{tr}}^-$ , the total flux, and the fraction of the flux carried in trapped modes all in one plot. As expected from their large vertical decay length, the least trapped modes at  $\omega, \kappa \rightarrow 0$  carry the least flux. The highest-frequency trapped modes carry a fraction of the total power that approaches 1, and the increase of this fraction with frequency or Bloch wavenumber is close to linear until an abrupt drop to zero at  $\omega > \omega_c$ . These “critically trapped” acoustic modes are the most efficient both at sucking power out of the source (given a fixed source amplitude), and at trapping this input power at the surface.

## 6. Conclusions and future work

We described a boundary integral equation method for solving the 2-dimensional, constant-coefficient Helmholtz equation on an exterior domain outside of an infinite, periodic boundary with corners. We did this in the context of acoustic scattering, with a particular emphasis on trapped modes. Using corner-refined Nyström quadrature on the boundary, we built a dense direct solver for the quasiperiodic problem. By integrating over the quasiperiodicity parameter, a method known as array scanning, we computed the scattering solution from a single point source, and extracted the limit of the acoustic pressure field infinitely far away from the source. Obtaining high-order accuracy required a detailed understanding of poles and branch-cuts, due to trapped modes and Wood anomalies respectively. To this end we proposed a complex contour deformation and nonuniform reparametrization for an efficient quadrature. We proposed a residue method to extract the amplitudes of left- and right-going trapped surface waves, and used this to study the fraction of injected acoustic power that ends up in trapped modes, as a function of frequency.

We show that the trapped modes (quasiperiodic eigenfunctions) map precisely to roots of a Fredholm determinant—see Theorem 4. By applying Nyström quadrature to this, we compute the trapped mode dispersion relation and group velocity. A simple ray model then allowed us to

predict frequency vs arrival time in the “chirp” phenomenon observed at *El Castillo* at Chichen Itza, and other similar acoustics recorded at step-temples.

Several questions remain for staircase acoustics: are there source locations close to the surface which excite trapped modes less, or excite the left- and right-going modes asymmetrically? Similarly, it would be of interest to extend the analysis to a wider range of periodic boundaries that possess asymmetry.

Although dense direct linear algebra as presented here was adequate for the studied geometry and accuracies, more complex geometries requiring more than  $10^4$  discretization nodes would benefit from the use of iterative solution with FMM acceleration. The extension to 3D doubly-periodic structures to high-order accuracy poses an interesting challenge, because there the set of Wood-anomaly on-surface wavevectors form curves.

## Acknowledgments

We are indebted to Eric J. Heller for suggesting that the raindrop effect is due to the dispersion relation of trapped evanescent waves; this motivated developing the methods presented here. We also thank Charlie Epstein, Manas Rachh, Leslie Greengard, and Simon Chandler-Wilde for their helpful comments and input. The Flatiron Institute is a division of the Simons Foundation.

## References

- [1] K. Busch, G. Von Freymann, S. Linden, S. Mingaleev, L. Tkeshelashvili, M. Wegener, Periodic nanostructures for photonics, *Physics Reports* 444 (3-6) (2007) 101–202.
- [2] J. D. Joannopoulos, S. G. Johnson, R. D. Meade, J. N. Winn, *Photonic Crystals: Molding the Flow of Light*, 2nd Edition, Princeton Univ. Press, Princeton, NJ, 2008.
- [3] Y. Chen, Y. Zhang, A. F. Koenderink, General point dipole theory for periodic metasurfaces: magnetoelectric scattering lattices coupled to planar photonic structures, *Opt. Express* 25 (18) (2017) 21358–21378.
- [4] G. Ji, J. Huber, Recent progress in acoustic metamaterials and active piezoelectric acoustic metamaterials—a review, *Applied Materials Today* 26 (2022) 101260.
- [5] J. Lin, H. Zhang, An integral equation method for numerical computation of scattering resonances in a narrow metallic slit, *J. Comput. Phys.* 385 (2019) 75–105.
- [6] B. Munk, G. Burrell, Plane-wave expansion for arrays of arbitrarily oriented piecewise linear elements and its application in determining the impedance of a single linear antenna in a lossy half-space, *IEEE transactions on antennas and propagation* 27 (3) (1979) 331–343.
- [7] Q.-Q. He, B.-Z. Wang, Radiation patterns synthesis for a conformal dipole antenna array, *Progress In Electromagnetics Research* 76 (2007) 327–340.
- [8] I. Herrero-Durá, A. Cebrecos, R. Picó, V. Romero-García, L. M. García-Raffi, V. J. Sánchez-Morcillo, Sound absorption and diffusion by 2D arrays of Helmholtz resonators, *Applied Sciences* 10 (5) (2020) 1690.
- [9] N. F. Declercq, C. S. Dekeyser, Acoustic diffraction effects at the Hellenistic amphitheater of Epidaurus: Seat rows responsible for the marvelous acoustics, *The Journal of the Acoustical Society of America* 121 (4) (2007) 2011–2022.
- [10] S. Shipman, Resonant scattering by open periodic waveguides, Vol. 1 of *Progress in Computational Physics (PiCP)*, Bentham Science Publishers, 2010, Ch. 2, pp. 7–50. doi:10.2174/978160805150211001010007.
- [11] S. N. Chandler-Wilde, I. G. Graham, S. Langdon, E. A. Spence, Numerical-asymptotic boundary integral methods in high-frequency acoustic scattering, *Acta numerica* 21 (2012) 89–305.
- [12] E. L. Richards, H. Song, W. Hodgkiss, Acoustic scattering comparison of Kirchhoff approximation to Rayleigh-fourier method for sinusoidal surface waves at low grazing angles, *The Journal of the Acoustical Society of America* 144 (3) (2018) 1269–1278.
- [13] N. Tsingos, S. Lefebvre, C. Dachsbacher, M. Dellepiane, Extending geometrical acoustics to highly detailed architectural environments, in: *19th International Congress on Acoustics (ICA 2007)*, 2007, p. 6.
- [14] J. A. C. Calleja, N. F. Declercq, The acoustic raindrop effect at Mexican pyramids: The architects’ homage to the rain god Chac?, *Acustica* 95 (2009) 849–856.



- [15] E. J. Heller, *Why You Hear What You Hear: An Experiential Approach to Sound, Music, and Psychoacoustics*, Princeton University Press, 2012.
- [16] D. Colton, R. Kress, *Inverse acoustic and electromagnetic scattering theory*, 2nd Edition, Vol. 93 of Applied Mathematical Sciences, Springer-Verlag, Berlin, 1998.
- [17] M. S. Howe, *Acoustics of fluid-structure interactions*, Cambridge University Press, 1998.
- [18] D. Colton, R. Kress, *Integral Equation Methods in Scattering Theory*, Society for Industrial and Applied Mathematics, Philadelphia, PA, 1983. doi:10.1137/1.9781611973167.
- [19] M. Kaltenbacher, *Computational acoustics*, Springer, 2018.
- [20] I. Rana, N. Alexopoulos, Current distribution and input impedance of printed dipoles, *IEEE Transactions on Antennas and Propagation* 29 (1) (1981) 99–105.
- [21] F. Capolino, D. R. Jackson, D. R. Wilton, Mode excitation from sources in two-dimensional EBG waveguides using the array scanning method, *IEEE Microwave and Wireless Components Letters* 15 (2) (2005) 49–51.
- [22] A. Lechleiter, R. Zhang, A convergent numerical scheme for scattering of aperiodic waves from periodic surfaces based on the Floquet–Bloch transform, *SIAM J. Numer. Anal.* 55 (2) (2017) 713–736.
- [23] R. Zhang, Numerical methods for scattering problems in periodic waveguides, *Numer. Math.* 148 (2021) 959–996. doi:10.1007/s00211-021-01229-0.
- [24] A.-S. Bonnet-BenDhia, F. Starling, Guided waves by electromagnetic gratings and non-uniqueness examples for the diffraction problem, *Math. Meth. Appl. Sci.* 17 (1994) 305–338.
- [25] C. H. Wilcox, *Scattering theory for diffraction gratings*, Applied Mathematical Sciences, volume 46, Springer-Verlag, 1984.
- [26] D. V. Evans, C. M. Linton, Edge waves along periodic coastlines, *Q. J. Mech. Appl. Math.* 46 (1993) 643–656.
- [27] V. Y. Gotlib, Solutions of the Helmholtz equation, concentrated near a plane periodic boundary, *J. Math. Sci.* 102 (2000) 4188–4194. doi:10.1007/BF02673850.
- [28] A. Kirsch, A. Lechleiter, The limiting absorption principle and a radiation condition for the scattering by a periodic layer, *SIAM J. Math. Anal.* 50 (3) (2017) 2536–65. doi:10.1137/17M1118920.
- [29] C. L. Epstein, Solving the transmission problem for open wave-guides. II outgoing estimates (2023). arXiv:2310.05816.
- [30] R. W. Wood, On a remarkable case of uneven distribution of light in a diffraction grating spectrum, *Philos. Mag.* 4 (1902) 396–408.
- [31] U. Fano, The theory of anomalous diffraction gratings and of quasi-stationary waves on metallic surfaces (Sommerfeld’s waves), *J. Opt. Soc. Am.* 31 (3) (1941) 213–222.
- [32] A. Hessel, A. Oliner, A new theory of Wood’s anomalies on optical gratings, *Appl. Opt.* 4 (10) (1965) 1275–1297.
- [33] T. Arens, S. N. Chandler-Wilde, J. A. DeSanto, On integral equation and least squares methods for scattering by diffraction gratings, *Commun. Comput. Phys.* 1 (2006) 1010–42.
- [34] O. P. Bruno, M. C. Haslam, Efficient high-order evaluation of scattering by periodic surfaces: deep gratings, high frequencies, and glancing incidences, *J. Opt. Soc. Am. A* 26 (3) (2009) 658–668.
- [35] A. Barnett, L. Greengard, A new integral representation for quasi-periodic scattering problems in two dimensions, *BIT Numerical mathematics* 51 (2011) 67–90.
- [36] O. P. Bruno, B. Delourme, Rapidly convergent two-dimensional quasi-periodic Green function throughout the spectrum—including Wood anomalies, *J. Comput. Phys.* 262 (2014) 262–290.
- [37] M. H. Cho, A. H. Barnett, Robust fast direct integral equation solver for quasi-periodic scattering problems with a large number of layers, *Optics express* 23 (2) (2015) 1775–1799.
- [38] R. Kress, V. Maz’ya, V. Kozlov, *Linear integral equations*, Vol. 82, Springer, 1989. doi:10.1007/978-1-4612-0559-3.
- [39] R. Zhang, A high order numerical method for scattering from locally perturbed periodic surfaces, *SIAM J. Sci. Comput.* 40 (4) (2018) A2286–A2314.
- [40] G. Fairweather, A. Karageorghis, The method of fundamental solutions for elliptic boundary value problems, *Advances in Computational Mathematics* 9 (1998) 69–95.
- [41] A. H. Cheng, Y. Hong, An overview of the method of fundamental solutions—solvability, uniqueness, convergence, and stability, *Engineering Analysis with Boundary Elements* 120 (2020) 118–152.
- [42] A. H. Barnett, T. Betcke, Stability and convergence of the method of fundamental solutions for helmholtz problems on analytic domains, *Journal of Computational Physics* 227 (14) (2008) 7003–7026.
- [43] C. J. Alves, S. S. Valtchev, Numerical comparison of two meshfree methods for acoustic wave scattering, *Engineering Analysis with Boundary Elements* 29 (4) (2005) 371–382.
- [44] R. Petit (Ed.), *Electromagnetic Theory of Gratings*, Vol. 22 of Topics in Current Physics, Springer-Verlag, Heidelberg, 1980.
- [45] R. Millar, The Rayleigh hypothesis and a related least-squares solution to scattering problems for periodic surfaces and other scatterers, *Radio Science* 8 (8-9) (1973) 785–796.
- [46] W. C. Meecham, On the use of the Kirchhoff approximation for the solution of reflection problems, *Journal of*

- Rational Mechanics and Analysis 5 (2) (1956) 323–334.
- [47] J. B. Keller, A geometrical theory of diffraction, in: L. M. Graves (Ed.), *Calculus of Variations and its Applications*, no. 8 in *Proceedings of Symposia in Applied Mathematics*, McGraw-Hill, New York, 1958, pp. 27–52.
- [48] J. B. Keller, Geometrical theory of diffraction, *Josa* 52 (2) (1962) 116–130.
- [49] C. M. Linton, The Green’s function for the two-dimensional Helmholtz equation in periodic domains, *J. Eng. Math.* 33 (1998) 377–402.
- [50] C. M. Linton, Lattice sums for the Helmholtz equation, *SIAM review* 52 (4) (2010) 630–674.
- [51] K. Yasumoto, K. Yoshitomi, Efficient calculation of lattice sums for free-space periodic Green’s function, *IEEE Transactions on Antennas and Propagation* 47 (6) (1999) 1050–1055.
- [52] J. L. Tsalamengas, Gauss–Jacobi quadratures for weakly, strongly, hyper-and nearly-singular integrals in boundary integral equation methods for domains with sharp edges and corners, *Journal of Computational Physics* 325 (2016) 338–357.
- [53] T. A. Driscoll, L. N. Trefethen, *Schwarz–Christoffel mapping*, Vol. 8, Cambridge University Press, 2002.
- [54] J. Bremer, V. Rokhlin, I. Sammis, Universal quadratures for boundary integral equations on two-dimensional domains with corners, *Journal of Computational Physics* 229 (22) (2010) 8259–8280.
- [55] J. Helsing, R. Ojala, Corner singularities for elliptic problems: Integral equations, graded meshes, quadrature, and compressed inverse preconditioning, *Journal of Computational Physics* 227 (20) (2008) 8820–8840.
- [56] A. Gopal, L. N. Trefethen, New Laplace and Helmholtz solvers, *Proceedings of the National Academy of Sciences* 116 (21) (2019) 10223–10225.
- [57] L. Zhao, A. H. Barnett, Robust and efficient solution of the drum problem via Nyström approximation of the Fredholm determinant, *SIAM J. Numer. Anal.* 53 (4) (2015) 1984–2007.
- [58] F. W. J. Olver, D. W. Lozier, R. F. Boisvert, C. W. Clark (Eds.), *NIST Handbook of Mathematical Functions*, Cambridge University Press, 2010.  
URL <http://dlmf.nist.gov>
- [59] L. N. Trefethen, *Approximation Theory and Approximation Practice*, Extended Edition, SIAM, 2019.
- [60] L. Greengard, K. L. Ho, J.-Y. Lee, A fast direct solver for scattering from periodic structures with multiple material interfaces in two dimensions, *Journal of Computational Physics* 258 (2014) 738–751.
- [61] K. E. Atkinson, *The numerical solution of integral equations of the second kind*, Cambridge University Press, 1997.
- [62] W. H. Press, *Numerical recipes 3rd edition: The art of scientific computing*, Cambridge university press, 2007.
- [63] A. Kirsch, Uniqueness theorems in inverse scattering theory for periodic structures, *Inv. Probs.* 10 (1) (1994) 145–152. doi:10.1088/0266-5611/10/1/011.
- [64] O. Bühler, *A Brief Introduction to Classical, Statistical, and Quantum Mechanics*, Courant Lecture Notes, AMS, 2006.
- [65] N. F. Declercq, J. Degrieck, R. Briers, O. Leroy, A theoretical study of special acoustic effects caused by the staircase of the El Castillo pyramid at the Maya ruins of Chichen-Itza in Mexico, *The Journal of the Acoustical Society of America* 116 (6) (2004) 3328–3335.
- [66] B. Bolotovskii, A. Lebedev, On threshold phenomena in classical electrodynamics, *Sov. Phys. JETP* 26 (4) (1968) 784–786.
- [67] C. C. Wojcik, H. Wang, M. Orenstein, S. Fan, Universal behavior of the scattering matrix near thresholds in photonics, *Physical Review Letters* 127 (27) (2021) 277401.
- [68] D. Huybrechs, R. Cools, On generalized Gaussian quadrature rules for singular and nearly singular integrals, *SIAM journal on numerical analysis* 47 (1) (2009) 719–739.
- [69] G. Lovat, R. Araneo, S. Celozzi, Dipole excitation of periodic metallic structures, *IEEE transactions on antennas and propagation* 59 (6) (2011) 2178–2187.
- [70] W. v. Ignatowsky, Reflexion elektromagnetisches Wellen an einem Draht, *Annalen der Physik* 323 (13) (1905) 495–522.
- [71] A. Sveshnikov, The radiation principle, in: *Dokl. Akad. Nauk SSSR*, Vol. 73, 1950, pp. 917–920.
- [72] A. H. Barnett, G. R. Marple, S. Veerapaneni, L. Zhao, A unified integral equation scheme for doubly periodic Laplace and Stokes boundary value problems in two dimensions, *Communications on Pure and Applied Mathematics* 71 (11) (2018) 2334–2380.